

Tracer transport in ICON

Scientific documentation

Daniel Reinert
Deutscher Wetterdienst
Abteilung Forschung und Entwicklung

Offenbach am Main, January 25, 2012

Contents

1	Tracer transport in ICONAM	1
1.1	Tracer equation	1
1.2	Finite-Volume (FV) discretization	2
1.2.1	Notation	2
1.2.2	Cell integrated version of the continuity equation	2
1.2.3	Fractional step implementation	3
1.3	Horizontal transport	5
1.3.1	Cell integrated version of the tracer continuity equation	5
1.3.2	Graphical interpretation	6
1.3.3	Basic algorithm	6
1.3.4	Reconstruction	7
	Least squares solution using SVD	7
1.3.5	Flux limiter (Flux corrected transport)	8
	Monotone (MO) limiter	8
	The Zalesak Corrector	9
	Positive definite (PD) limiter	10
1.3.6	Results	11
	Solid body advection	11
	\mathcal{C}^1 Cosine bell	11
	\mathcal{C}^3 Cosine bell	12
	\mathcal{C}^1 Cosine bell: Courant number dependency	14
	Deformational flow	15
	Deformational flow: Courant number dependency	18
1.4	Vertical transport	20
1.4.1	MUSCL	20
	Mathematical formulation	20
1.4.2	Piecewise parabolic method (PPM)	26
	Mathematical formulation	26
1.5	Reduced calling frequency	34
2	Tracer transport in ICOHAM	37
3	Transport	39
3.1	Argument lists	39
	Bibliography	45

Chapter 1

Tracer transport in ICONAM

The transport package predicts the large-scale re-distribution of tracers (e.g. water substances, trace gases) caused by air-motions. Mathematically (numerically) this is done by solving one of the fundamental laws of physics, namely the equation of mass continuity for each tracer.

1.1 Tracer equation

In ICONAM a height-based coordinate system is applied. The continuity equation that is solved numerically reads

$$\frac{\partial \rho_m q}{\partial t} + \nabla \cdot (\rho_m q \mathbf{v}) = P_{\rho_m q}, \quad (1.1)$$

where ρ_m denotes the density of moist air, \mathbf{v} is the 3D velocity vector $(u, v, w)^T$, t is the time, $\nabla \cdot$ represents a multidimensional flux divergence, and q denotes the specific tracer concentration which is defined as follows:

$$q_\chi = \frac{m_\chi}{m_d + m_v}. \quad (1.2)$$

m_χ is the mass of the tracer species χ and m_d , m_v denote the mass of dry air and water vapour, respectively. By setting $q = 1$ in (1.1) we recover the continuity equation for moist air

$$\frac{\partial \rho_m}{\partial t} + \nabla \cdot (\rho_m \mathbf{v}) = P_{\rho_m}, \quad (1.3)$$

The property of (1.1) to reduce to (1.3) for $q = 1$ is sometimes termed *tracer and air mass consistency*. Care must be taken to retain this property in the discretization.

In the most recent version of ICONAM (version 1.2.2) we solve prognostic continuity equations of type (1.1) for 5 water species: water vapour q_v , cloud water q_c , rain water q_r , cloud ice q_i and snow q_s .

In the following we will respectively use ρ and q to denote moist air density and the specific tracer concentration. Moreover, since the focus of this documentation is on the transport process itself, any sources or sinks will be neglected, i.e.

$$P_{\rho q} = 0. \quad (1.4)$$

The incorporation of a nonzero rhs is described in the physics documentation.

1.2 Finite-Volume (FV) discretization

The numerical solution to the continuity equation (1.1) is based on so called space-time finite volume methods. By space-time methods we refer to methods, where the temporal and spacial discretizations are combined rather than separated. Space-time methods are also known as *cell-integrated semi-Lagrangian* schemes. As will become clear, the applied schemes are neither purely semi-Lagrangian, nor Eulerian in the classical sense. They are Eulerian in the sense that we consider the flux of mass through the stationary cell walls. On the other hand they are not Eulerian in the sense, that typically the space and time discretizations are separated. They are semi-Lagrangian in the sense that trajectory calculations are needed for flux computation. The schemes that will be presented could be termed *flux form semi-Lagrangian*. They are partly based on work by Lauritzen et al. (2010), Harris and Lauritzen (2010), Skamarock and Menchaca (2010), Miura (2007) and Colella and Woodward (1984).

1.2.1 Notation

In the recent version of ICONAM the continuity equation for tracer mass is discretized on the triangular grid, thus assuming triangular control volumes (CVs). The normal velocities $v_{n,e,k}$ are given at edge midpoints and the specific concentration q_{ik} is given at cell circumcenters (see Fig. ??). The index i denotes the grid-cell and the index k denotes the vertical (full) level, numbered in top-to-bottom order. Thus $k - 1/2$ and $k + 1/2$ denote the upper and lower vertical half-level, respectively. Note that q is considered as an average over a prismatic cell rather than as discrete point value.

$$\bar{q}_{ik}^n = \frac{1}{\Delta V_i} \iiint_{V_i} q(x, y, z, t^n) dV \quad (1.5)$$

Here, $q(x, y, z, t^n)$ denotes the (usually unknown) subgrid scale distribution of q and ΔV_i is the volume of a prismatic cell. The superscript n denotes the time step t^n and the overbar denotes the (known) cell average.

1.2.2 Cell integrated version of the continuity equation

A cell-integrated solution to the continuity equation (1.1) can formally be derived, by integrating (1.1) over the 3D control volume i and in time over the time interval $[t^n, t^{n+1}]$, with $t^{n+1} - t^n = \Delta t$.

$$\begin{aligned} \int_{t^n}^{t^{n+1}} \iint_{A_i} \int_{z_{k+\frac{1}{2}}}^{z_{k-\frac{1}{2}}} \frac{\partial(\rho q)}{\partial t} dt dA dz = & - \int_{t^n}^{t^{n+1}} \iint_{A_i} \int_{z_{k+\frac{1}{2}}}^{z_{k-\frac{1}{2}}} \nabla_h \cdot (\rho q \mathbf{v}_h) dt dA dz \\ & - \int_{t^n}^{t^{n+1}} \iint_{A_i} \int_{z_{k+\frac{1}{2}}}^{z_{k-\frac{1}{2}}} \frac{\partial}{\partial z} (\rho q w) dt dA dz \end{aligned} \quad (1.6)$$

Here, A_i denotes the horizontal area of the prism (triangle) and Δz_k the prism thickness. The index h indicates horizontal 2D operators and vectors. Commuting differentiation and

integration on the lhs as well as applying Gauss-Theorem on the rhs leads to

$$\begin{aligned} (\overline{\rho q} \Delta A \Delta z)_{i,k}^{n+1} - (\overline{\rho q} \Delta A \Delta z)_{i,k}^n = & - \int_{t^n}^{t^{n+1}} \oint_{\partial A_i} (\overline{\rho q \mathbf{v}_h^z})_k \cdot \mathbf{n} \Delta z_k \, dl \, dt \\ & - \int_{t^n}^{t^{n+1}} \left[(\overline{\rho q w^h})_{i,k-\frac{1}{2}} - (\overline{\rho q w^h})_{i,k+\frac{1}{2}} \right] \Delta A_i \, dt, \end{aligned} \quad (1.7)$$

where \mathbf{n} is the outward pointing normal vector along the boundary of A_i and ${}^{-z}$, ${}^{-h}$ indicates vertical and horizontal averages, respectively, for the given grid cell. Noting that the boundary integral can be split into 3 integrals along the triangle edges and that ΔA_i is time independent as well as independent of the vertical level k , equation (1.7) can be further simplified:

$$\begin{aligned} (\overline{\rho q} \Delta z)_{i,k}^{n+1} = (\overline{\rho q} \Delta z)_{i,k}^n - \frac{1}{\Delta A_i} \sum_{e=1}^{N_e} \int_{l_e} \int_{t^n}^{t^{n+1}} (\Delta z \overline{\rho q \mathbf{v}_h^z} \cdot \mathbf{n})_{e,k} \, dl \, dt \\ - \int_{t^n}^{t^{n+1}} \left[(\overline{\rho q w^h})_{i,k-\frac{1}{2}} - (\overline{\rho q w^h})_{i,k+\frac{1}{2}} \right] \, dt, \end{aligned} \quad (1.8)$$

N_e is the number of edges (currently $N_e = 3$). Schematically the partial density $\overline{\rho q}_{i,k}^{n+1}$ at the new time step $n + 1$ is given by

$$\overline{\rho q}_{i,k}^{n+1} = \overline{\rho q}_{i,k}^n + \Delta t [\mathcal{H}(q^n) + \mathcal{V}(q^n)], \quad (1.9)$$

where \mathcal{H} and \mathcal{V} denote horizontal and vertical operators, with

$$\mathcal{H}(q^n) = - \frac{1}{\Delta t \Delta A_i \Delta z_k} \sum_{e=1}^{N_e} \int_{l_e} \int_{t^n}^{t^{n+1}} (\Delta z \overline{\rho q \mathbf{v}_h^z} \cdot \mathbf{n})_{e,k} \, dl \, dt \quad (1.10)$$

$$\mathcal{V}(q^n) = - \frac{1}{\Delta t \Delta z_k} \int_{t^n}^{t^{n+1}} \left[(\overline{\rho q w^h})_{i,k-\frac{1}{2}} - (\overline{\rho q w^h})_{i,k+\frac{1}{2}} \right] \, dt. \quad (1.11)$$

The operators \mathcal{H} and \mathcal{V} denote the horizontal and vertical flux divergence, respectively. As will become clear, both operators only act on $q^n(x, y, z)$ and adopt the mass fluxes as provided by the dynamical core. The solution procedure for equation (1.9) will be presented in the following section.

1.2.3 Fractional step implementation

Instead of solving the unwieldy equation (1.9) in one sweep, the problem is splitted into two simpler sub-problems, that are solved individually, using different numerical algorithms. As already indicated by equation (1.9), instead of solving the fully 3D transport problem, we individually solve one transport problem for the vertical and one for the horizontal direction. This technique is known as directional splitting. Of course, replacing the equation

$$\overline{\rho q}_{i,k}^{n+1} = \overline{\rho q}_{i,k}^n + \Delta t [\mathcal{H}(q^n) + \mathcal{V}(q^n)] \quad (1.12)$$

by some approximation involving the two subproblems

$$\overline{\rho q}_{i,k}^{n+1} = \overline{\rho q}_{i,k}^n + \Delta t \mathcal{V}(q^n) \quad (1.13)$$

$$\overline{\rho q}_{i,k}^{n+1} = \overline{\rho q}_{i,k}^n + \Delta t \mathcal{H}(q^n) \quad (1.14)$$

will inevitably result in a residual error. This error is known as the *splitting error*.

We follow the formulation of Easter (1993), wherein the mass conservation equation (1.3) is reintegrated using the mass fluxes provided by the dynamical core. The 3D algorithm is as follows:

$$\overline{\rho q}_{i,k}^* = \overline{\rho q}_{i,k}^n + \Delta t \mathcal{V}(\bar{q}^n) \quad (1.15)$$

$$\overline{\rho}_{i,k}^* = \overline{\rho}_{i,k}^n + \Delta t \mathcal{V}(1) \quad (1.16)$$

$$\bar{q}_{i,k}^* = \frac{\overline{\rho q}_{i,k}^*}{\overline{\rho}_{i,k}^*} \quad (1.17)$$

$$(1.18)$$

$$\overline{\rho q}_{i,k}^{n+1} = \overline{\rho q}_{i,k}^* + \Delta t \mathcal{H}(\bar{q}^*) \quad (1.19)$$

$$\overline{\rho}_{i,k}^{n+1} = \overline{\rho}_{i,k}^* + \Delta t \mathcal{H}(1) \quad (1.20)$$

$$\bar{q}_{i,k}^{n+1} = \frac{\overline{\rho q}_{i,k}^{n+1}}{\overline{\rho}_{i,k}^{n+1}} \quad (1.21)$$

The splitting error of this so called *Marchuk-splitting* is of $\mathcal{O}(\Delta t)$. A *Strang-splitting* (which results in an $\mathcal{O}(\Delta t^2)$ approximation to (1.9)) can approximately be achieved by switching the order each time step. A full *Strang-splitting* has been implemented, too. It is given by the following sequence of operations:

$$\overline{\rho q}_{i,k}^* = \overline{\rho q}_{i,k}^n + \Delta t/2 \mathcal{V}(\bar{q}^n) \quad (1.22)$$

$$\overline{\rho}_{i,k}^* = \overline{\rho}_{i,k}^n + \Delta t/2 \mathcal{V}(1) \quad (1.23)$$

$$\bar{q}_{i,k}^* = \frac{\overline{\rho q}_{i,k}^*}{\overline{\rho}_{i,k}^*} \quad (1.24)$$

$$(1.25)$$

$$\overline{\rho q}_{i,k}^{**} = \overline{\rho q}_{i,k}^* + \Delta t \mathcal{H}(\bar{q}^*) \quad (1.26)$$

$$\overline{\rho}_{i,k}^{**} = \overline{\rho}_{i,k}^* + \Delta t \mathcal{H}(1) \quad (1.27)$$

$$\bar{q}_{i,k}^{**} = \frac{\overline{\rho q}_{i,k}^{**}}{\overline{\rho}_{i,k}^{**}} \quad (1.28)$$

$$(1.29)$$

$$\overline{\rho q}_{i,k}^{n+1} = \overline{\rho q}_{i,k}^n + \Delta t/2 \mathcal{V}(\bar{q}^{**}) \quad (1.30)$$

$$\overline{\rho}_{i,k}^{n+1} = \overline{\rho}_{i,k}^n + \Delta t/2 \mathcal{V}(1) \quad (1.31)$$

$$\bar{q}_{i,k}^{n+1} = \frac{\overline{\rho q}_{i,k}^{n+1}}{\overline{\rho}_{i,k}^{n+1}} \quad (1.32)$$

1.3 Horizontal transport

The horizontal transport scheme of ICON belongs to the class of so called **Flux Form Semi-Lagrangian** (FFSL) schemes. Sometimes these schemes are alternatively termed *Incremental remapping schemes* (Lipscomb and Ringler, 2005) or *schemes based on the streamline subgrid integration method* (Yeh, 2007).

1.3.1 Cell integrated version of the tracer continuity equation

The current scheme is based on a finite volume (or cell integrated) version of the horizontal tracer continuity equation in flux form

$$\frac{\partial \rho q}{\partial t} = -\nabla_h \cdot (\rho q \mathbf{v}_h) , \quad (1.33)$$

where ρ is the air density, q is the tracer mixing ratio and \mathbf{v}_h is the 2D horizontal velocity vector. According to (1.8), the finite volume version of the horizontal tracer continuity equation can be written as follows:

$$(\overline{\rho q} \Delta z)_i^{n+1} - (\overline{\rho q} \Delta z)_i^n = -\frac{1}{\Delta A_i} \sum_{e=1}^{N_e} \int_{l_i^e} \int_{t^n}^{t^{n+1}} (\Delta z \overline{\rho q \mathbf{v}_h^z} \cdot \mathbf{n})_e \, dl \, dt \quad (1.34)$$

In practice, ρ is replaced by its cell-height weighted counterpart $\rho \Delta z$. Here, for convenience, we will simply drop Δz . Furthermore we will drop the vertical averaging operator $\overline{}$.

Now we introduce our first approximation: We assume that ρ is constant along the edge and constant over the time step Δt . Or stated in another way: We assume that an appropriate space-time averaged value of ρ is provided by the dycore). Thus we may shift ρ in front of the integrals, as follows:

$$(\overline{\rho q_i^{n+1}} - \overline{\rho q_i^n}) \Delta A_i = -\sum_{e=1}^{N_e} \langle \overline{\rho_i^e} \rangle \int_{l_i^e} \int_{t^n}^{t^{n+1}} (q \mathbf{v}_h \cdot \mathbf{n})_e \, dl \, dt \quad (1.35)$$

Here we have introduced the operators $\overline{}$ and $\langle \rangle$ which indicate averages along the edge and in time, respectively. Note that the time integral may also be performed in space along the trajectories terminating at the control volume edge, such that the scheme may finally be cast into the following form

$$\overline{\rho q_i^{n+1}} = \overline{\rho q_i^n} - \frac{1}{\Delta A_i} \sum_{e=1}^{N_e} s_{ie} F_{ie} \quad , \text{ with } F_{ie} = \langle \overline{\rho_i^e} \rangle \iint_{a_i^e} q^n(x, y) \, da . \quad (1.36)$$

F_{ie} defines the total mass crossing edge e during Δt and a_i^e denotes the so called *departure region area* for the e^{th} edge. The departure region is spanned by the edge e and the two backward trajectories that end at the vertices belonging to that edge at t^{n+1} . s_i^e distinguishes inward and outward directed fluxes and is defined as follows:

$$s_i^e = \mathbf{N}^e \cdot \mathbf{n}_i^e = \begin{cases} 1 & : \text{ for outward directed fluxes} \\ -1 & : \text{ for inward directed fluxes} \end{cases} \quad (1.37)$$

Here \mathbf{n}_i^e denotes the unit vector at edge e pointing in the outward normal direction of cell i and \mathbf{N}^e is the normal vector at edge e . If we define i^e as the cell sharing edge e with cell i , \mathbf{N}^e points from i to i^e .

Comment: Re-write in such a way that the approximation regarding ρ comes afterwards.

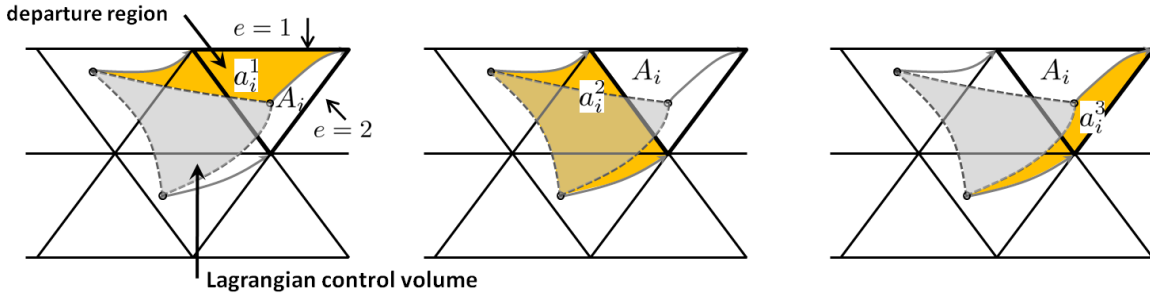


Figure 1.1: graphical interpretation of the FFSL scheme. Black solid lines show the primal grid, with thick solid lines indicating the Eulerian control volume, grey area shows Lagrangian control volume and yellow areas show departure regions for each edge.

1.3.2 Graphical interpretation

Figure 1.1 provides a graphical interpretation of the FFSL-scheme. Black solid lines show the primal grid, with thick solid lines indicating the selected Eulerian control volume of area ΔA_i . Let us assume that we know the full time dependent velocity field such that we know the trajectories of all the air parcels terminating at the control volume edges at the new time t^{n+1} . As an example, the trajectories of the air parcels which terminate at the control volume vertices at the new time t^{n+1} are indicated by grey lines. Accordingly assume that we know the starting points of those backward trajectories at time t^n . With this information one can construct the Lagrangian control volume, also known as 'departure cell'. It is depicted in grey. This departure cell (at time t^n) is mapped onto our control volume at time t_{n+1} . In a standard semi-Lagrangian scheme, in order to compute the updated value of $\bar{\rho q}$ for the Eulerian control volume, one needs to compute the total mass inside the departure cell. Since we apply the Eulerian instead of the semi-Lagrangian viewpoint, according to equation (1.36), we need to compute the total tracer mass F that crosses each of the Eulerian control volume edges during the time interval $[t, t + \Delta t]$. This mass is simply the material present in the yellow regions, termed departure regions, shown in Figure 1.1. These regions are swept across the e^{th} edge by the corresponding e^{th} edge of the Lagrangian control volume (departure cell). For each edge the integration areas are highlighted in yellow.

Note that this Eulerian viewpoint is fully equivalent to the semi-Lagrangian viewpoint. It can be shown (Lauritzen et al., 2011) that all areas involved in our quasi-Eulerian forecast equation (1.36) sum up to the Lagrangian control volume.

1.3.3 Basic algorithm

The numerical algorithm solving (1.36) for a single Eulerian control volume proceeds in 4 major stages:

1. The departure regions a_i^e for each edge are approximated with the help of backward trajectories.
2. For each Eulerian control volume the unknown tracer subgrid distribution $q(x, y, t_0)$ is estimated from the known cell averages \bar{q}_i^n of the CV itself and surrounding cells.
3. The total mass crossing the e^{th} edge is estimated by evaluating the integral in (1.36). I.e. the estimated subgrid distribution $q(x, y, t_0)$ is integrated over the approximated departure region a_i^e .

4. Evaluate the sum on the right hand side of (1.36) (i.e. compute net mass gain/loss of cell i) in order to arrive at an updated value of $\bar{\rho q}$.

1.3.4 Reconstruction

Least squares solution using SVD

The question we would like to answer is: *What is the minimal length least squares solution of the overdetermined system*

$$\mathbf{A} \cdot \mathbf{x} = \mathbf{b}, \quad (1.38)$$

where \mathbf{A} is the $m \times n$ design matrix with $m > n$, \mathbf{x} is the unknown solution vector (polynomial coefficients) of dimension n and \mathbf{b} (of dimension m) contains the known parameters to be fitted. That means, we search for the vector \mathbf{x} that minimizes the squared Euclidian norm of the residual

$$\mathbf{r} = \mathbf{b} - \mathbf{A} \cdot \mathbf{x} \quad (1.39)$$

$$\min_{\mathbf{x}} \|\mathbf{r}\|_2^2 = \min_{\mathbf{x}} \|\mathbf{b} - \mathbf{A} \cdot \mathbf{x}\|_2^2 \quad (1.40)$$

This minimal length vector \mathbf{x} can be found by using the so called *Singular Value Decomposition* (SVD).

Theorem 1 (proof see Golub and Loan (1996)). *Let $\mathbf{A} \in \mathbb{R}^{m \times n}$ with $m > n$ be a matrix of rank r . Then there exist orthogonal matrices $\mathbf{U} \in \mathbb{R}^{m \times m}$ and $\mathbf{V} \in \mathbb{R}^{n \times n}$ such that*

$$\mathbf{A} = \mathbf{U} \mathbf{\Sigma} \mathbf{V}^T, \quad \mathbf{\Sigma} = \begin{pmatrix} \mathbf{\Sigma}_1 & 0 \\ 0 & 0 \end{pmatrix},$$

where $\mathbf{\Sigma} \in \mathbb{R}^{m \times n}$, $\mathbf{\Sigma}_1 = \text{diag}(\sigma_1, \sigma_2, \dots, \sigma_r)$, and $\sigma_1 \geq \sigma_2 \geq \dots \geq \sigma_r > 0$. The σ_i are called the singular values of \mathbf{A} .

Based in this theorem, equation (1.38) can be re-written as follows:

$$(\mathbf{U} \mathbf{\Sigma} \mathbf{V}^T) \cdot \mathbf{x} = \mathbf{b} \quad (1.41)$$

Solving (1.41) for the unknown \mathbf{x} gives

$$\mathbf{x} = \mathbf{A}^+ \mathbf{b} \quad , \quad \text{with} \quad \mathbf{A}^+ = \mathbf{V} \mathbf{\Sigma}^{-1} \mathbf{U}^T. \quad (1.42)$$

\mathbf{A}^+ is called the *pseudoinverse* or *Moore-Penrose inverse* of \mathbf{A} . The pseudoinverse always exists whether or not \mathbf{A} is a square matrix or has full rank. The nice thing about SVD is, that (1.42) immediately provides the minimum norm least squares solution! **For any \mathbf{b} in \mathbb{R}^m , $\mathbf{A}^+ \mathbf{b}$ is the minimum norm least squares solution to (1.38).**

For SVD we use the lapack routine DGESDD. After the matrixes $\mathbf{U} \mathbf{\Sigma} \mathbf{V}^T$ are known, the pseudoinverse is computed element-wise as follows:

$$\mathbf{A}_{ij}^+ = \left(\mathbf{V} \mathbf{\Sigma}^{-1} \mathbf{U}^T \right)_{ij} = \sum_k \mathbf{V}_{ki}^T \mathbf{\Sigma}_{kk}^{-1} \mathbf{U}_{jk} \quad (1.43)$$

Since \mathbf{A}^+ is time independent and independent of the tracer fields, it is computed once during startup and stored for future use.

1.3.5 Flux imiter (Flux corrected transport)

The basic idea of the *flux corrected transport* (FCT) approach is to construct the transportive flux for a given edge as the weighted average of a flux computed by a low order (monotone) scheme and a flux computed by a high order scheme. The aim is to make use of the high order flux to the greatest extent possible, without generating over- and undershoots in the solution. FCT goes back to the pioneering work of Boris and Book (1973) and was further generalized by Zalesak (1979).

Monotone (MO) limiter

The implementation largely follows the general procedure described in Zalesak (1979).

1. **For all edges in the domain, high order fluxes F_e^H are computed** by using the FFSL-scheme as presented in Sec. 1.3.1.

$$F_e^H = F_e^M \bar{q}_i^{a_i^{e,n}}, \quad (1.44)$$

where F_e^M denotes the mass flux for edge e , which is provided by the dynamical core, and $\bar{q}_i^{a_i^{e,n}}$ denotes a higher order approximation of the tracer field averaged over the flux region a_i^e at time step n .

2. **For all edges in the domain, low order fluxes F_e^L are computed** as

$$F_e^L = F_e^M \bar{q}_u^n, \quad (1.45)$$

where F_e^M , again, denotes the mass flux for edge e , and \bar{q}_u^n is the cell average of the upwind cell at time step n .

3. **Define anti-diffusive fluxes over all edges in the domain**

$$A_e = F_e^H - F_e^L \quad (1.46)$$

For each cell i these fluxes are grouped into fluxes going out (positive) and into (negative) the cell.

4. **Compute a monotone estimate of the solution**

$$\bar{q}_i^{L, n+1} = \frac{\bar{\rho} \bar{q}_i^n}{\bar{\rho}_i^{n+1}} - \frac{\Delta t}{\bar{\rho}_i^{n+1} \Delta A_i} \sum_{e=1}^{N_e} s_{ie} l_i^e F_e^L \quad (1.47)$$

5. **Clip antidiffusive fluxes** so that the following “antidiffusion” step does not generate new extrema (maxima or minima), or amplifies existing ones.

$$A_e^c = C_e A_e \quad 0 \leq C_e \leq 1 \quad (1.48)$$

6. **Construct the net transportive (limited) flux and compute the final solution**

$$F_e^c = F_e^L + A_e^c \quad (1.49)$$

$$= (1 - C_e) F_e^L + C_e F_e^H \quad (1.50)$$

Note that the net transportive flux F_e equals the high order flux F_e^H for $C_e = 1$, and equals the low order flux F_e^L for $C_e = 0$. The final solution \bar{q}^{n+1} is computed outside of the FCT-routine, using the limited fluxes F_e^c .

The critical step is of course the computation of the Zalesak-Corrector C_e (step 5), which will be described in the next paragraph.

The Zalesak Corrector

For each cell i two different correctors C_i^\pm are computed - one for outgoing (C_i^-) and one for incoming (C_i^+) antidiffusive fluxes. When computing C_i^- it is assumed that all incoming antidiffusive fluxes are zero. The opposite assumption holds for C_i^+ . Note that this is a worst case scenario. As a result the limiter is sub-optimal in the sense that antidiffusive fluxes are limited more than necessary and the solution is overly damped. For a possible iterative improvement of the Zalesak Correctors see (). The corrector for incoming fluxes is computed as follows:

1. Compute the sum of all incoming antidiffusive fluxes for cell i

$$P_i^+ = -1 \sum_{e=1}^{N_e} \min(0, \tilde{A}_e) \quad (1.51)$$

Note, that incoming fluxes are negative, while outgoing fluxes are positive. Also note that for convenience, A_e is replaced by \tilde{A}_e which has been multiplied by a geometrical factor, such that it has the dimensions of a mixing ratio [kg/kg] rather than a flux [kg/(m²s)].

$$\tilde{A}_e = \frac{\Delta t l_e}{\Delta A_i \bar{\rho}_i^{n+1}} A_e \quad (1.52)$$

2. Compute the maximum mass change Δq_i^+ that is allowed to be caused by the incoming antidiffusive fluxes. Exceeding this change of mass will introduce new extrema in \bar{q}_i^{n+1} which have not already been present in \bar{q}_i^n or the low order solution $\bar{q}_i^{L, n+1}$. Define

$$\Phi_i^a = \max(\bar{q}_i^n, \bar{q}_i^{L, n+1}) \quad (1.53)$$

to let

$$\Delta q_i^+ = \max(\Phi_i^a, \Phi_{n1}^a, \Phi_{n2}^a, \Phi_{n3}^a) - \bar{q}_i^{L, n+1}, \quad (1.54)$$

where $n1, n2, n3$ indicate the direct neighbors of cell i . If $P_i^+ > \Delta q_i^+$, the incoming antidiffusive fluxes need to be rescaled (clipped) using the following factor:

$$C_i^+ = \begin{cases} \min\left(1, \frac{\Delta q_i^+}{(P_i^+ + \epsilon)}\right) & : \text{ if } P_i^+ > 0 \\ 0 & : \text{ if } P_i^+ = 0 \end{cases} \quad (1.55)$$

The corresponding quantities for outgoing antidiffusive fluxes read:

$$P_i^- = \sum_{e=1}^{N_e} \max(0, \tilde{A}_e) \quad (1.56)$$

$$\Phi_i^b = \min(\bar{q}_i^n, \bar{q}_i^{L, n+1}) \quad (1.57)$$

$$\Delta q_i^- = \bar{q}_i^{L, n+1} - \min(\Phi_i^b, \Phi_{n1}^b, \Phi_{n2}^b, \Phi_{n3}^b) \quad (1.58)$$

$$C_i^- = \begin{cases} \min\left(1, \frac{\Delta q_i^-}{(P_i^- + \epsilon)}\right) & : \text{ if } P_i^- > 0 \\ 0 & : \text{ if } P_i^- = 0 \end{cases} \quad (1.59)$$

In a last step, limit the antidiffusive flux A_e so that it neither produces overshoots in the cell into which it is directed, nor undershoots in the cell out of which it flows. To this end, the smallest Zalesak-Corrector needs to be selected from the cells upwind and downwind of the given edge.

$$C_e = \min(C_u^-, C_d^+) \quad (1.60)$$

Here, the indices u, d indicate the cells upwind and downwind of the given edge.

Positive definite (PD) limiter

Our positive definite limiter is based on a modification/simplification of the monotone limiter described in section 1.3.5. In order to render any high-order flux form scheme positive definite, the following inequality must be fulfilled for each cell:

$$\frac{1}{\Delta A_i} \sum_{e=1}^{N_e} s_i^e F_i^e \leq \overline{\rho' q_i^n}, \quad (1.61)$$

It states that the mass lost by cell i during Δt must be equal to or smaller than the total mass within cell i at the previous time step n . If this constraint is violated for cell i , all outgoing fluxes have to be re-scaled accordingly.

The PD-limiter is implemented as follows: For each cell i the sum of all outward fluxes F_i^e is computed.

$$P_i^- = \frac{1}{\Delta A_i} \sum_{e=1}^{N_e} \max(0, s_i^e F_i^e) \quad (1.62)$$

The maximum outward flux permitted is given by

$$Q_i^- = \overline{\rho' q_i^n}. \quad (1.63)$$

Note that this is a worst case scenario, since it implies that $P_i^+ = 0$ i.e. that there is no inward flux. As a result, the limiter is sub-optimal in the sense that outward fluxes are re-scaled more than necessary and the solution is overly damped. As a next step a correction factor R_i^- is computed based on constraint (1.61).

$$R_i^- = \begin{cases} \min\left(1, \frac{Q_i^-}{(P_i^- + \epsilon)}\right) & : \text{ if } P_i^- > 0 \\ 1 & : \text{ if } P_i^- = 0 \end{cases} \quad (1.64)$$

Then the edge-based correction factor becomes

$$C_e^- = \begin{cases} R_i^- & : \text{ if } \text{sgn}(v_n \bar{q}^e) \geq 0 \\ R_{i^e}^- & : \text{ if } \text{sgn}(v_n \bar{q}^e) < 0 \end{cases} \quad (1.65)$$

Note: As pointed out by Harris and Lauritzen (2010) and Thuburn and McIntyre (1997) positive-definite methods do not preserve linear correlations.

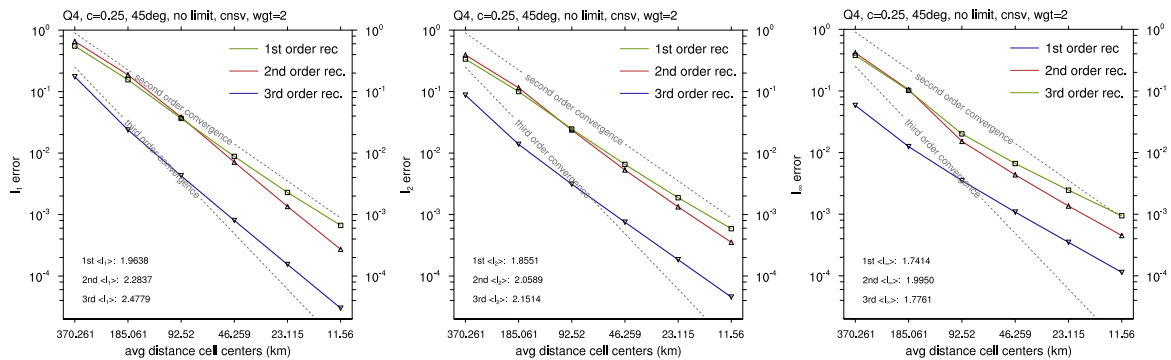


Figure 1.2: Error norms L_1 , L_2 and L_∞ for the \mathcal{C}^1 bell as a function of average grid spacing. Numbers in legends correspond to empirically determined convergence rates \mathcal{L}_1 , \mathcal{L}_2 , \mathcal{L}_∞ . Grey lines correspond to the slopes of second and third-order convergence rates.

1.3.6 Results

Solid body advection

\mathcal{C}^1 Cosine bell

The initial condition is a cosine bell, defined as

$$\Psi(\lambda, \theta) = \begin{cases} \frac{\Psi_0}{2} (1 + \cos(\pi r/R)) & \text{if } r < R \\ 0 & \text{otherwise,} \end{cases} \quad (1.66)$$

where $\Psi_0 = 1$, $R = a/3$ is the bell radius, a is the radius of the sphere, and r is the great-circle distance between (λ, θ) and the distribution center (λ_c, θ_c) .

The initial condition has continuous first order derivatives (i.e. is \mathcal{C}^1). The average Courant number is about 0.25. The initial condition will be advected once around the sphere, using $\varphi = \pi/4$, where φ is the rotation angle of the flow (0 for zonal flow, $\pi/2$ for flow over the pole).

In Fig. 1.2 convergence rates of L_1 , L_2 and L_∞ are shown for a 1st order (linear), second order (quadratic) and third order (cubic) reconstruction. For the quadratic and cubic case a conservative reconstruction has been used, while the linear case is based on a non-conservative reconstruction. The non-conservative linear reconstruction was found to slightly outperform the conservative one. The test case was initialized by integrating the analytical function (1.67) over each triangular element using a 4th order accurate Gauss-Legendre quadrature.

When initializing the testcases, care has to be taken that a sufficiently accurate estimate of the cell averages is provided. As highlighted in Fig. 1.3, the results clearly depend on the initialization procedure. If the tracer field is initialized using the point values evaluated at cell circumcenters, then the convergence rates start to deviate from the expected convergence rates as we go to higher resolutions. The higher the order of the polynomial reconstruction, the larger the deviation. The results clearly show, that it is not sufficient to initialize the model with point values evaluated at cell circumcenters. This merely gives a zeroth order estimate of the cell average. A second order accurate estimate of the cell average seems to be sufficient, even for a cubic reconstruction.

Figure 1.4 is the same as Fig. 1.2, but with the monotone flux limiter switched on. Surprisingly, the 2nd order (quadratic) reconstruction performs best in this case. The cubic reconstruction suffers from excessive damping, when using the monotone limiter. These

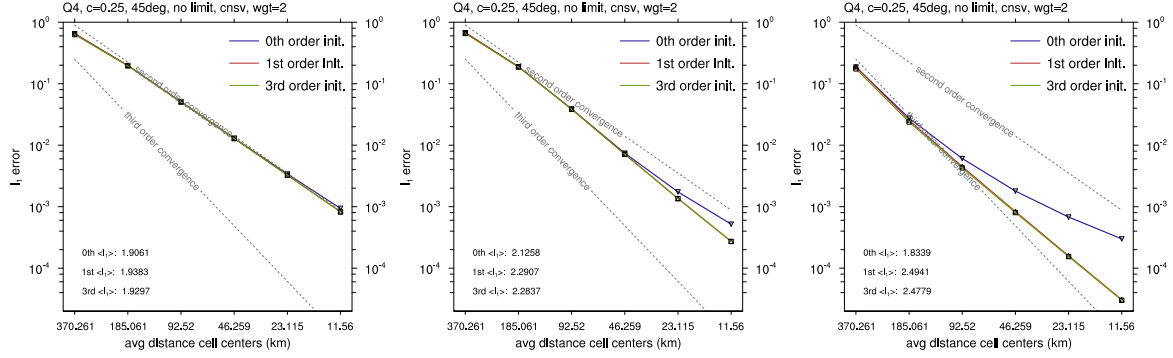


Figure 1.3: L_1 norm for the \mathcal{C}^1 bell as a function of average grid spacing. (a) linear, (b) quadratic, (c) cubic reconstruction. Different colors refer to different initialization procedures of different accuracy. blue: 0th order, red: 1st order, green: 3rd order accurate initialization.

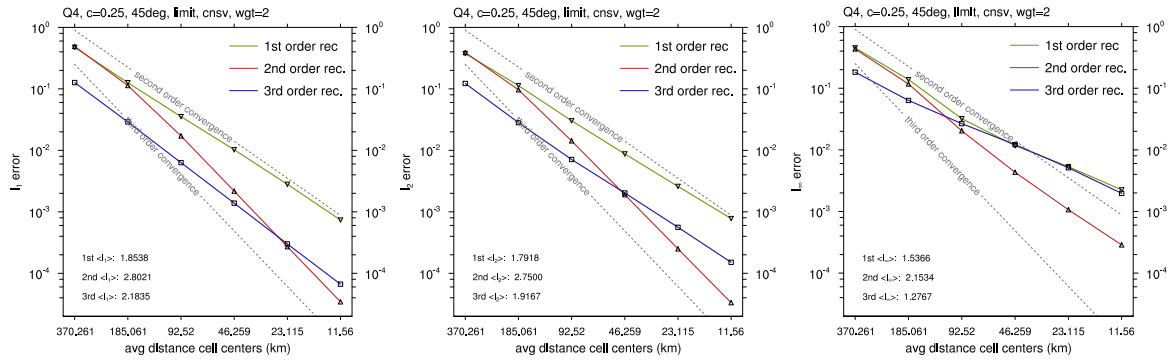


Figure 1.4: Error norms L_1 , L_2 and L_∞ for the \mathcal{C}^1 bell as a function of average grid spacing. With monotone flux limiter. Numbers in legends correspond to empirically determined convergence rates \mathcal{L}_1 , \mathcal{L}_2 , \mathcal{L}_∞ . Grey lines correspond to the slopes of second and third-order convergence rates.

results are based on a 4th order accurate initialization procedure. Again, the results change only marginally if we apply a 2nd order accurate initialization procedure (not shown).

Figure 1.5 is the same as Fig. 1.4, but with the positive definite instead of the monotone limiter switched on. The results are based on a 4th order accurate initialization procedure. Again, the 2nd order reconstruction performs best. The 1st order non-conservative reconstruction slightly outperformed the conservative one (not shown). In Fig. 1.5 only the non-conservative one is shown.

\mathcal{C}^3 Cosine bell

The \mathcal{C}^1 bell does not provide a true estimate of the 'optimal' convergence rate for the schemes with quadratic and cubic reconstruction. Determining the order of accuracy for these two schemes assumes a solution with at least smooth second and third order derivatives, respectively. Therefore we reconducted the simulations using the following modified initial condition:

$$\Psi(\lambda, \theta) = \begin{cases} \frac{\Psi_0}{4} (1 + \cos(\pi r/R))^2 & \text{if } r < R \\ 0 & \text{otherwise,} \end{cases} \quad (1.67)$$

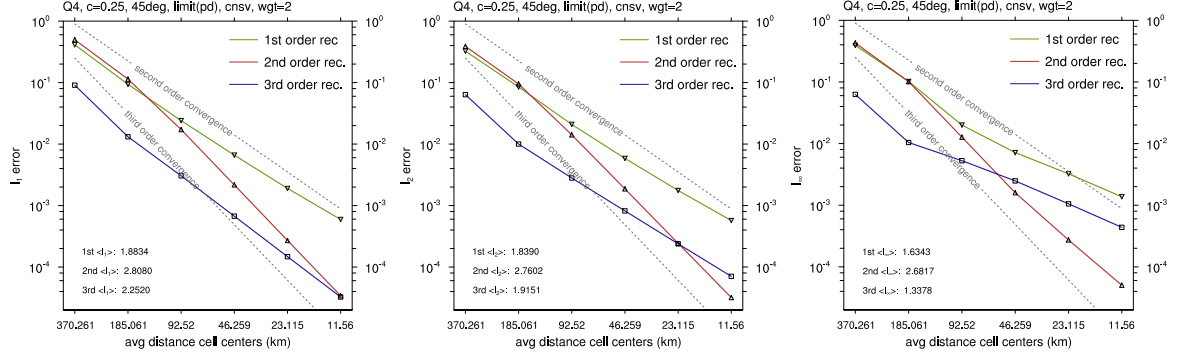


Figure 1.5: Error norms L_1 , L_2 and L_∞ for the \mathcal{C}^1 bell as a function of average grid spacing. With positive definite flux limiter. A non-conservative reconstruction was used for the first order one. Numbers in legends correspond to empirically determined convergence rates \mathcal{L}_1 , \mathcal{L}_2 , \mathcal{L}_∞ . Grey lines correspond to the slopes of second and third-order convergence rates.

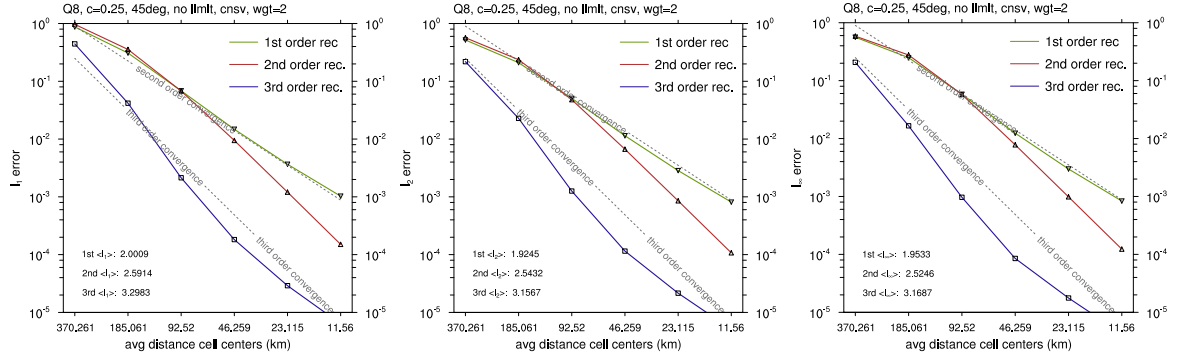


Figure 1.6: Error norms L_1 , L_2 and L_∞ for the \mathcal{C}^3 bell as a function of average grid spacing without flux limiter. A non-conservative reconstruction was used for the first order one. Numbers in legends correspond to empirically determined convergence rates \mathcal{L}_1 , \mathcal{L}_2 , \mathcal{L}_∞ . Grey lines correspond to the slopes of second and third-order convergence rates.

where $\Psi_0 = 1$, $R = a/3$ is the bell radius, a is the radius of the sphere, and r is the great-circle distance between (λ, θ) and the distribution center (λ_c, θ_c) . This initial condition has continuous second and third order derivatives. The average Courant number is the same as in Sec. 1.3.6 (i.e. $c = 0.25$).

Figure 1.6 shows error norms for the \mathcal{C}^3 bell without any limiter. The linear and quadratic scheme both show the expected second and third order convergence rates, respectively, in all three error norms. This also holds for the conservative linear scheme, although the conservative scheme, again, gives slightly higher absolute errors (not shown). The unlimited cubic scheme, however, does not converge at the theoretically expected 4th order for very high resolutions. This even holds, if we push the accuracy of the initialization procedure beyond second order (the \mathcal{C}^3 bell may still be not smooth enough?). Nevertheless, the cubic scheme gives the most accurate results in terms of absolute errors over the entire resolution range tested.

Figure 1.7 shows the resolution dependency of the errors when the monotone limiter is switched on. For the linear scheme, the rate of convergence and the absolute errors are barely affected by the limiter. For the quadratic method converges at a slower rate (somewhat less than third order), which is most notably pronounced for the L_∞ error. For the cubic method

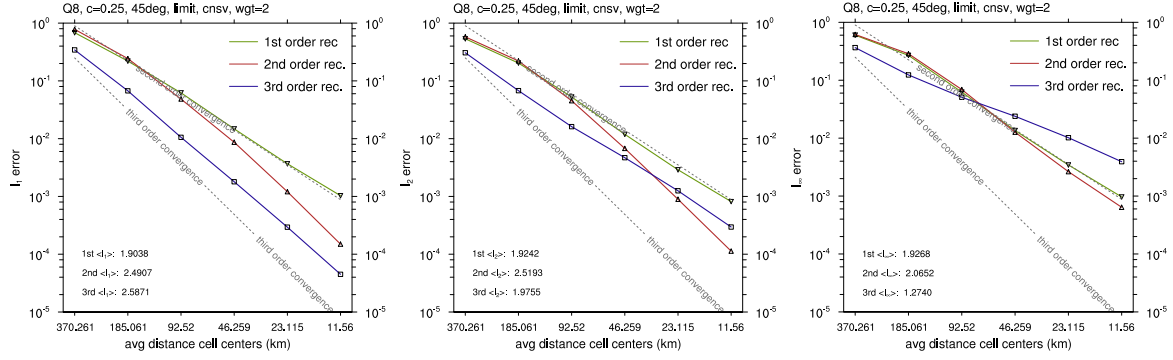


Figure 1.7: Error norms L_1 , L_2 and L_∞ for the \mathcal{C}^3 bell as a function of average grid spacing with monotone flux limiter. A non-conservative reconstruction was used for the first order one. Numbers in legends correspond to empirically determined convergence rates \mathcal{L}_1 , \mathcal{L}_2 , \mathcal{L}_∞ . Grey lines correspond to the slopes of second and third-order convergence rates.

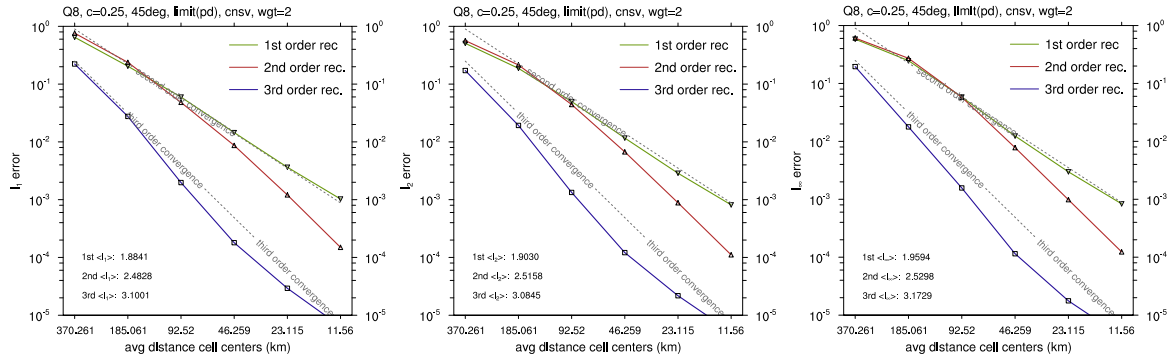


Figure 1.8: Error norms L_1 , L_2 and L_∞ for the \mathcal{C}^3 bell as a function of average grid spacing with positive definite flux limiter. A non-conservative reconstruction was used for the first order one. Numbers in legends correspond to empirically determined convergence rates \mathcal{L}_1 , \mathcal{L}_2 , \mathcal{L}_∞ . Grey lines correspond to the slopes of second and third-order convergence rates.

we see a dramatic decrease in the convergence rate of L_∞ and L_2 , which drops towards 1st and 2nd order, respectively.

The performance of the cubic scheme greatly improves, if the less restrictive positive definite limiter is applied. This can be inferred from Fig. 1.8. Independent of the applied reconstruction order, the results closely resemble those of the unlimited scheme (compare with Fig. 1.6).

\mathcal{C}^1 Cosine bell: Courant number dependency

To see how the error evolves with changing Courant numbers, the solid body advection test has been repeated on the $R2B5$ grid using variable timesteps. Furthermore this will give insight into the stability limit of the various schemes. The timestep ranges from $50\text{ s} < \Delta t < 1620\text{ s}$, which is equivalent to Courant numbers in the range $0.028 < c < 0.9$.

In Fig. 1.9 L_2 and L_∞ error norms for first, second and third order reconstructions are shown after a single revolution of the \mathcal{C}^1 cosine bell using a variable timestep. No limiter was applied. The left figure shows results for a flow rotation angle of $\varphi = \pi/4$, while for the figure on the right hand side $\varphi = 0$ was used. Let us have a closer look at the results for $\varphi = \pi/4$.

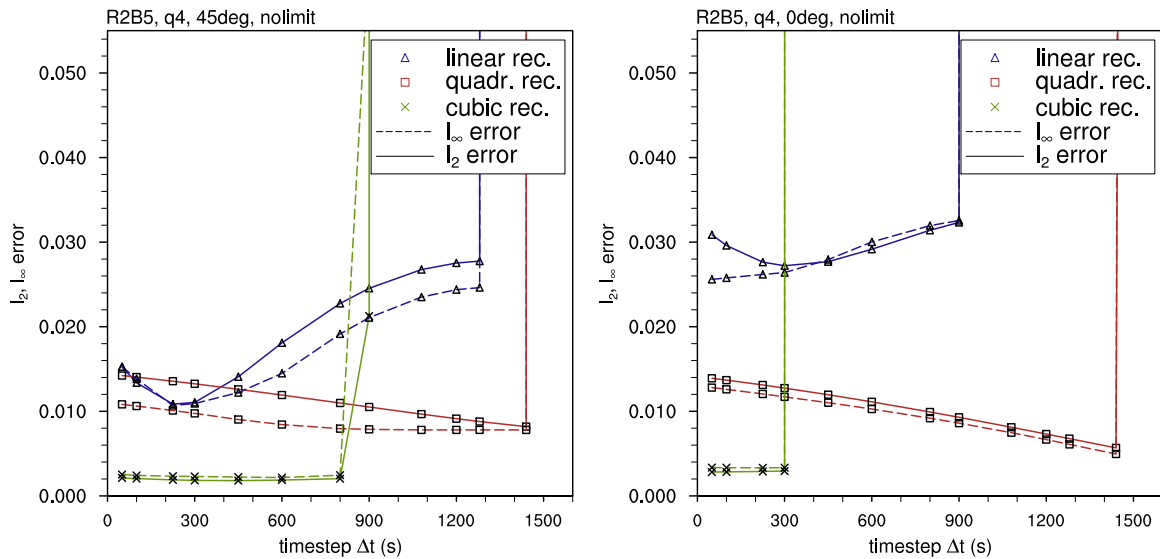


Figure 1.9: L_2 and L_∞ error norms for first (blue), second (red) and third (green) order reconstructions after a single revolution of the C^1 cosine bell using a variable timestep on the R2B5 grid. (a) flow rotation angle $\varphi = \pi/4$, (b) flow rotation angle $\varphi = 0$.

For Courant numbers larger than about $c \approx 0.15$, the linear scheme exhibits increasing errors with increasing Courant numbers. The opposite holds for the quadratic scheme, whereas the cubic scheme exhibits almost no Courant number dependency of the absolute error. Over most of the investigated Courant number range, the linear scheme produces the largest errors, followed by the quadratic scheme. The cubic scheme produces the lowest errors. Regarding numerical stability, we see that the cubic scheme already becomes unstable for $c \gtrsim 0.45$. The linear scheme becomes unstable for $c \gtrsim 0.7$ whereas the quadratic scheme remains stable up to $c \lesssim 0.8$.

Similar results are shown in Fig. 1.10 but with the monotone limiter switched on. Note that for the quadratic scheme, the absolute errors decrease for the particular test case if the limiter is switched on. The opposite is true for the cubic scheme.

To see how the error changes, if we change the path along which the tracer bell is advected, the simulation has been reconducted using $\varphi = 0$ (see Fig. 1.9, right). We see, that for the linear scheme the absolute error depends quite strongly on the path, which is not the case for the quadratic and cubic scheme. This setup seems to be quite challenging, since the range of stable CFL numbers shrinks for both the linear and cubic scheme. The cubic scheme already becomes unstable for $c \gtrsim 0.25$. The linear scheme becomes unstable for $c \gtrsim 0.5$.

Deformational flow

Recently Nair and Lauritzen (2010) introduced a new deformational flow benchmark test for advection schemes on the sphere. The flow is strongly deformational, nondivergent and the scalar field follows highly complex trajectories. The flow reverses its course at half time $T/2$ and the tracer, ideally, returns back to its initial position and shape. There is the possibility of cancellations of errors due to reversal of the flow along the same trajectories. This can be avoided by adding a solid body rotation, such that the tracer follows new trajectories after the flow reversal.

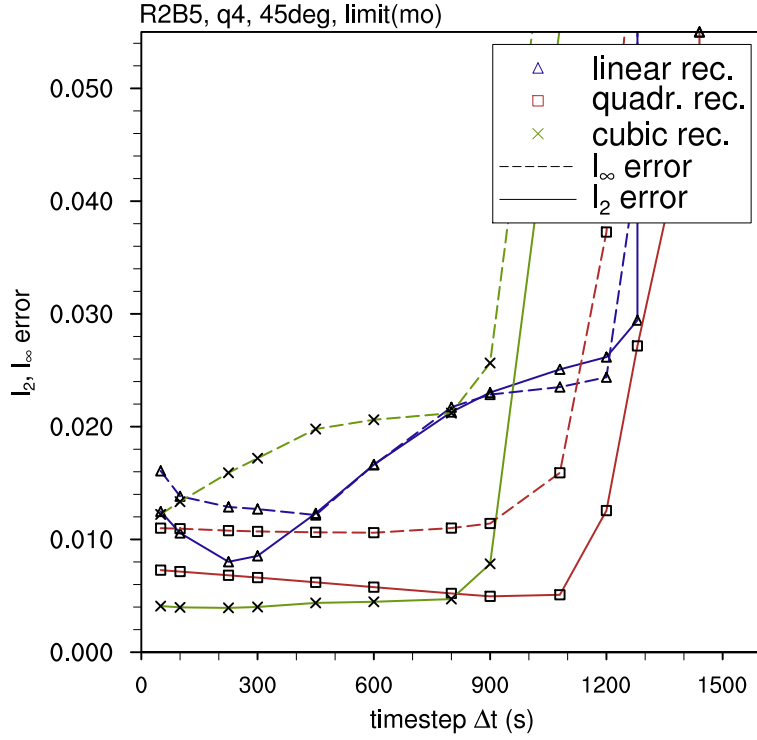


Figure 1.10: L_2 and L_∞ error norms for first (blue), second (red) and third (green) order reconstructions after a single revolution of the C^1 cosine bell using a variable timestep on the R2B5 grid. A monotone flux limiter has been applied.

For air density the initial condition is $\rho(t = 0) = 1 \text{ kg m}^{-3}$. For the tracer mixing ratio Ψ two different initial conditions have been tested: a C^1 cosine bell and an infinitely smooth C^∞ Gaussian hill.

Two symmetrically located cosine bells are defined as follows:

$$h_i(\lambda, \theta) = \frac{h_{max}}{2} [1 + \cos(\pi r_i/R)] \quad \text{if } r_i < R, \quad (1.68)$$

where $h_{max} = 1$, $R = 1/2$ is the bell radius, and r_i is the great-circle distance between (λ, θ) and the specified center of the bell (λ_i, θ_i) . The initial condition consists of a background value b and two cosine bells with centers (λ_i, θ_i) , $i = 1, 2$ generated using (1.68).

$$\Psi(\lambda, \theta) = \begin{cases} b + c h_1(\lambda, \theta) & \text{if } r_1 < R \\ b + c h_2(\lambda, \theta) & \text{if } r_2 < R \\ 0 & \text{otherwise,} \end{cases} \quad (1.69)$$

with $b = 0$ and $c = 1$.

The second initial condition is a smooth 2D Gaussian surface following Levy et al. (2007) that can be defined as follows,

$$h_i(\lambda, \theta) = h_{max} \exp\left(-b_0 \left[(x - x_i)^2 + (y - y_i)^2 + (z - z_i)^2\right]\right), \quad (1.70)$$

where (x, y, z) defines the 3D cartesian coordinates corresponding to the spherical coordinates (λ, θ) , h_{max} is the height of the hill and $b_0 = 5$ defines the width. Again, the initial distribuiotn

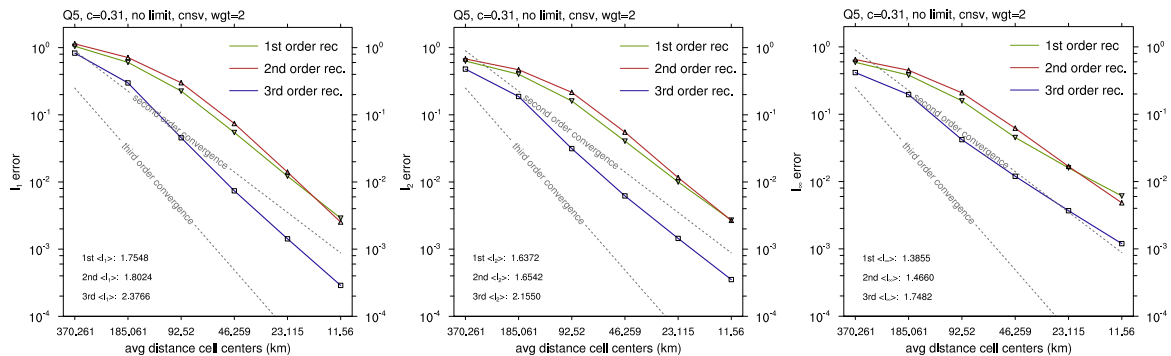


Figure 1.11: Error norms L_1 , L_2 and L_∞ for the C^1 cosine bell as a function of average grid spacing without limiter. A non-conservative reconstruction was used for the first order one. Numbers in legends correspond to empirically determined convergence rates \mathcal{L}_1 , \mathcal{L}_2 , \mathcal{L}_∞ . Grey lines correspond to the slopes of second and third-order convergence rates.

consists of two hills h_1 and h_2 using (1.70),

$$\Psi(\lambda, \theta) = h_1(\lambda, \theta) + h_2(\lambda, \theta). \quad (1.71)$$

The simulations with infinitely smooth (Gaussian hills) initial conditions should provide a numerical estimate of the optimal convergence rate of the scheme. In Fig. 1.11 the resolution dependency of the error is shown for the cosine bell initial condition. The red curve shows results for a non-conservative linear reconstruction, blue for a conservative quadratic and green for a conservative cubic one. The Courant number was set to $c \approx 0.31$. The runs were performed without any limiting/filtering. As for the solid body test case, the cubic reconstruction, again, shows the smallest absolute error and largest convergence rate in all norms. For L_1 the convergence rate is slightly better than 2^{nd} order, for L_2 almost equal to 2^{nd} order and for L_∞ slightly worse than 2^{nd} order. The linear and quadratic reconstruction show very similar convergence rates, but at higher absolute errors. Surprisingly, the quadratic reconstruction does not lead to reduced absolute errors when compared to the linear reconstruction. At medium resolutions, the absolute errors are even slightly higher than for the linear reconstruction. Only for very high resolutions, the quadratic reconstruction seems to become superior compared to the linear reconstruction due to slightly better convergence rates.

In Fig. 1.12 same results are shown, but for a conservative linear reconstruction. The non-conservative linear reconstruction appears to be slightly superior to the conservative counterpart. The Green-Gauss reconstruction has been tested as well. Its performance is comparable to the non-conservative linear least squares reconstruction.

In Fig. 1.13 results are shown for the infinitely smooth (Gaussian hill) initial conditions. For the linear reconstruction the theoretically expected 2^{nd} order convergence rate is apparent in all norms. For very high resolutions, the convergence rate for the quadratic reconstruction tends towards third order. At medium resolution, the cubic reconstruction shows similar convergence rate. For very high resolutions, the convergence rates of the cubic reconstruction significantly degrade. The reason for that is not clear, yet. Anyhow, for the entire resolution range tested, the cubic reconstruction exhibits by far the smallest absolute errors. Once again, the quadratic reconstruction does not exhibit reduced absolute error when compared to the linear reconstruction. Only for very high resolutions, the quadratic reconstruction becomes superior in terms of absolute error.

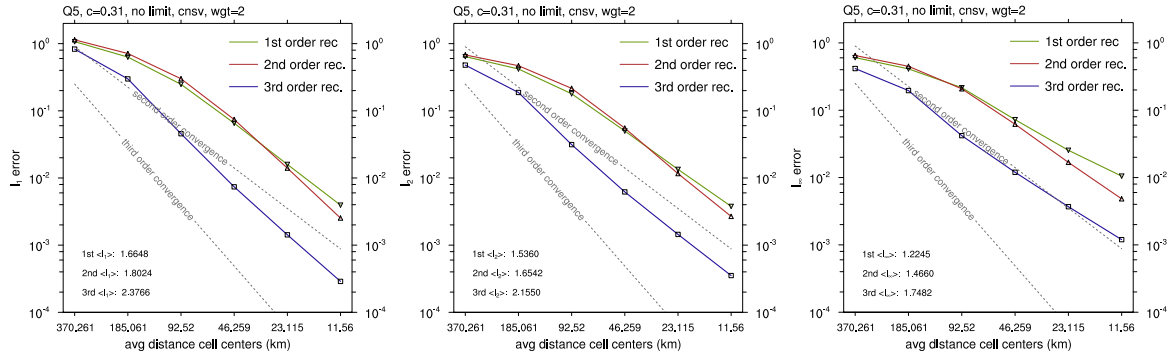


Figure 1.12: Error norms L_1 , L_2 and L_∞ for the C^1 cosine bell as a function of average grid spacing without limiter. A conservative reconstruction was used for the first order one. Numbers in legends correspond to empirically determined convergence rates \mathcal{L}_1 , \mathcal{L}_2 , \mathcal{L}_∞ . Grey lines correspond to the slopes of second and third-order convergence rates.

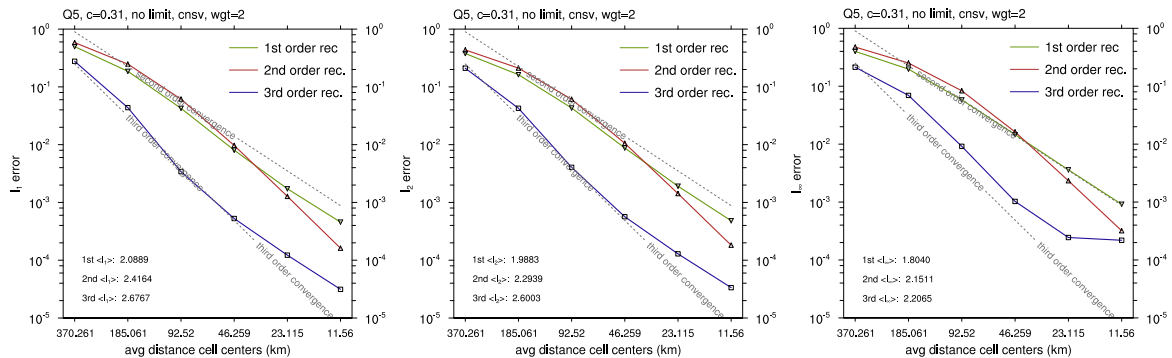


Figure 1.13: Error norms L_1 , L_2 and L_∞ for the C^∞ Gaussian hill as a function of average grid spacing without limiter. A non-conservative reconstruction was used for the first order one. Numbers in legends correspond to empirically determined convergence rates \mathcal{L}_1 , \mathcal{L}_2 , \mathcal{L}_∞ . Grey lines correspond to the slopes of second and third-order convergence rates.

Deformational flow: Courant number dependency

To see how the error evolves with varying Courant numbers, the deformational flow test case (DF4) has been repeated on the *R2B5* grid using variable timesteps. Furthermore, this test will give insight into the stability limit of the various schemes. The timestep ranges from $40\text{ s} < \Delta t < 800\text{ s}$, which corresponds to Courant numbers in the range $0.052 < c < 1.034$.

In Fig. 1.14 L_2 and L_∞ error norms for first, second and third order reconstructions are shown after one period of the DF4-test case as a function of timestep Δt . No limiter was applied. Basically the same Courant-Number dependency is found as for the solid body advection test (compare with Fig. 1.9). For Courant numbers larger than about $c \approx 0.2$, the linear scheme exhibits increasing errors with increasing Courant numbers. The opposite holds for the quadratic scheme, which shows slightly decreasing errors for increasing Courant numbers. Almost no Courant number dependency is found for the cubic scheme. In contrast to the solid body test case, now the quadratic scheme produces the largest errors, followed by the linear scheme. Once again, the cubic scheme produces by far the lowest errors. The comparatively high errors of the quadratic scheme may be related to the fact, that for large parts of the total simulation time, the Courant numbers are significantly lower than the

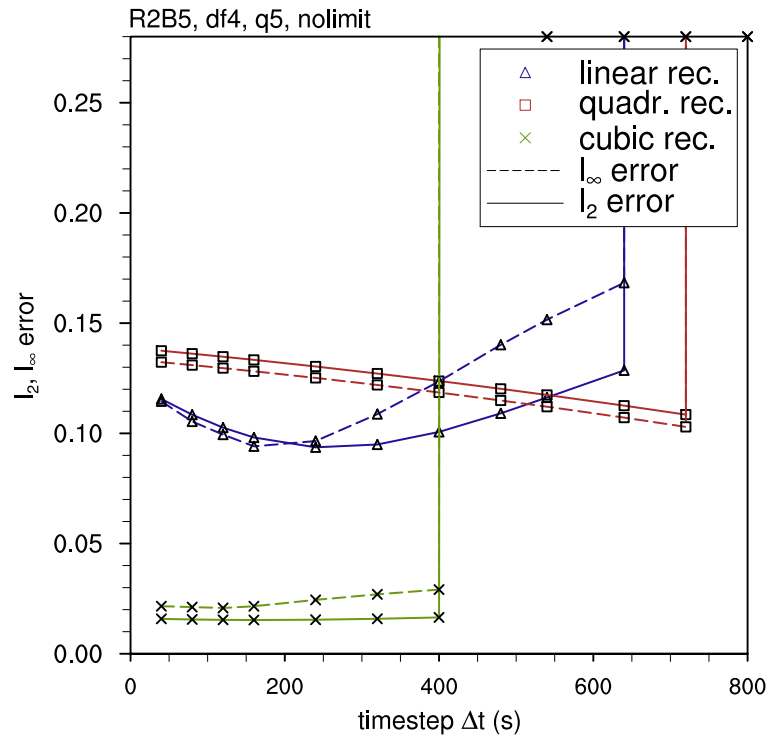


Figure 1.14: L_2 and L_∞ error norms for first (blue), second (red) and third (green) order reconstructions after one period of the deformational flow test case (DF4), using a variable timestep on the R2B5 grid. No limiting/filtering has been applied.

maximum numbers given above. This is related to the time dependent velocity field and is one of the mayor differences compared to the solid body test case. When combined with the Courant number dependency of the quadratic scheme shown in Fig. 1.14 this may (to some degree) explain the high errors of the quadratic scheme.

Regarding numerical stability, the quadratic scheme, again, shows the largest stability range, followed closely by the linear scheme. The quadratic scheme becomes unstable for $c_{max} \gtrsim 0.95$ and the linear scheme for $c_{max} \gtrsim 0.85$. As for the solid body rotation test caes, the cubic scheme shows the smallest stability range. It becomes unstable for $c_{max} \gtrsim 0.52$.

1.4 Vertical transport

1.4.1 MUSCL

Mathematical formulation

Table 1.1 compares the second order vertical advection scheme for ICOHAM and ICONAM. The Courant number independent version is shown in Table 1.2.

Table 1.1: Comparison of MUSCL vertical advection for ICOHAM and ICONAM

part	ICOHAM	ICONAM
Time discretization	$\bar{q}_k^{n+1} = \bar{q}_k^n \frac{\Delta p_k^n}{\Delta p_k^{n+1}} - \frac{\Delta t}{\Delta p_k^{n+1}} \left[F_{k+\frac{1}{2}}^n - F_{k-\frac{1}{2}}^n \right]$	$\bar{q}_k^{n+1} = \bar{q}_k^n \frac{\bar{\rho}_k^n \Delta z_k}{\bar{\rho}_k^{n+1} \Delta z_k} - \frac{\Delta t}{\bar{\rho}_k^{n+1} \Delta z_k} \left[F_{k-\frac{1}{2}}^n - F_{k+\frac{1}{2}}^n \right]$
vertical velocity	$w_\eta = \dot{\eta} \frac{\partial p}{\partial \eta}$	$w = \dot{z}$
cell height	$\Delta p_k^n = p_{k+\frac{1}{2}}^n - p_{k-\frac{1}{2}}^n$	$\Delta z_k = z_{k-\frac{1}{2}} - z_{k+\frac{1}{2}}$
Fluxes	$\mathbf{w}_\eta < \mathbf{0}$ ($\mathbf{w} > \mathbf{0}$, physical upwelling)	$\mathbf{w} > \mathbf{0}$, physical upwelling
	$F_{k-\frac{1}{2}}^n = w_{\eta, k-\frac{1}{2}}^{n+\alpha} \left[\bar{q}_k^n - \frac{1}{2} \frac{\partial q}{\partial p} \Big _k^n \Delta p_k^n \left(1 - C_{k-\frac{1}{2}}^+ \right) \right]$ $C_{k-\frac{1}{2}}^+ = \frac{w_{\eta, k-\frac{1}{2}}^{n+\alpha} \Delta t}{\Delta p_k^n}$	$F_{k-\frac{1}{2}}^n = \bar{\rho}_{k-\frac{1}{2}}^{n+1/2} w_{k-\frac{1}{2}}^{n+1/2} \left[\bar{q}_k^n + \frac{1}{2} \frac{\partial q}{\partial z} \Big _k^n \Delta z_k^n \left(1 - C_{k-\frac{1}{2}}^+ \right) \right]$ $C_{k-\frac{1}{2}}^+ = \frac{w_{k-\frac{1}{2}}^{n+1/2} \Delta t}{\Delta z_k^n}$
	$\mathbf{w}_\eta > \mathbf{0}$ ($\mathbf{w} < \mathbf{0}$, physical downwelling)	$\mathbf{w} < \mathbf{0}$, physical downwelling
	$F_{k-\frac{1}{2}}^n = w_{\eta, k-\frac{1}{2}}^{n+\alpha} \left[\bar{q}_{k-1}^n + \frac{1}{2} \frac{\partial q}{\partial p} \Big _{k-1}^n \Delta p_{k-1}^n \left(1 - C_{k-\frac{1}{2}}^- \right) \right]$ $C_{k-\frac{1}{2}}^- = \frac{w_{\eta, k-\frac{1}{2}}^{n+\alpha} \Delta t}{\Delta p_{k-1}^n}$	$F_{k-\frac{1}{2}}^n = \bar{\rho}_{k-\frac{1}{2}}^{n+1/2} w_{k-\frac{1}{2}}^{n+1/2} \left[\bar{q}_{k-1}^n - \frac{1}{2} \frac{\partial q}{\partial z} \Big _{k-1}^n \Delta z_{k-1}^n \left(1 - C_{k-\frac{1}{2}}^- \right) \right]$ $C_{k-\frac{1}{2}}^- = \frac{w_{k-\frac{1}{2}}^{n+1/2} \Delta t}{\Delta z_{k-1}^n}$

continued

Table 1.1: Comparison of MUSCL vertical advection for ICOHAM and ICONAM

part	ICOHAM	ICONAM
vertical gradient	$\left. \frac{\partial q}{\partial p} \right _k^n = \frac{q_{k+\frac{1}{2}}^n - q_{k-\frac{1}{2}}^n}{\Delta p_k^n}$	$\left. \frac{\partial q}{\partial z} \right _k^n = \frac{q_{k-\frac{1}{2}}^n - q_{k+\frac{1}{2}}^n}{\Delta z_k}$
linear interpolation from full level to half level	$q_{k-\frac{1}{2}}^n = \alpha_{k-\frac{1}{2}}^+ q_k^n + \alpha_{k-\frac{1}{2}}^- q_{k-1}^n$	$q_{k-\frac{1}{2}}^n = \alpha_{k-\frac{1}{2}}^+ q_k^n + \alpha_{k-\frac{1}{2}}^- q_{k-1}^n$
	$\alpha_{k-\frac{1}{2}}^+ = \frac{p_{k-\frac{1}{2}} - p_{k-1}}{p_k - p_{k-1}}$	$\alpha_{k-\frac{1}{2}}^+ = \frac{z_{k-1} - z_{k-\frac{1}{2}}}{z_{k-1} - z_k}$
	$\alpha_{k-\frac{1}{2}}^- + \alpha_{k-\frac{1}{2}}^+ = 1$	$\alpha_{k-\frac{1}{2}}^- + \alpha_{k-\frac{1}{2}}^+ = 1$

Table 1.2: Courant number independent version of vertical MUSCL for ICOHAM and ICONAM

part	ICOHAM	ICONAM
Time discretization	$\bar{q}_k^{n+1} = \bar{q}_k^n \frac{\Delta p_k^n}{\Delta p_k^{n+1}} - \frac{\Delta t}{\Delta p_k^{n+1}} \left[F_{k+\frac{1}{2}}^n - F_{k-\frac{1}{2}}^n \right]$	$\bar{q}_k^{n+1} = \bar{q}_k^n \frac{\bar{\rho}_k^n \Delta z_k}{\bar{\rho}_k^{n+1} \Delta z_k} - \frac{\Delta t}{\bar{\rho}_k^{n+1} \Delta z_k} \left[F_{k-\frac{1}{2}}^n - F_{k+\frac{1}{2}}^n \right]$
vertical velocity	$w_\eta = \eta \frac{\partial p}{\partial \eta}$	$w = \dot{z}$
cell height	$\Delta p_k^n = p_{k+\frac{1}{2}}^n - p_{k-\frac{1}{2}}^n$	$\Delta z_k = z_{k-\frac{1}{2}} - z_{k+\frac{1}{2}}$
Fluxes	<p>$\mathbf{w}_\eta < \mathbf{0}$ ($\mathbf{w} > \mathbf{0}$, physical upwelling)</p> $F_{k-\frac{1}{2}}^n = \sum_{l=0}^{K_{k-1/2}^+ - 1} \left(-\frac{\bar{q}_{k+l} \Delta p_{k+l}}{\Delta t} \right) - \frac{\Delta p_{k+K_{k-1/2}^+}}{\Delta t} C_{k-1/2}^{+K^+}$ $\left[\bar{q}_{k+K_{k-1/2}^+}^n - \frac{1}{2} \frac{\partial q}{\partial p} \Big _{k+K_{k-1/2}^+} \Delta p_{k+K_{k-1/2}^+} \left(1 - C_{k-\frac{1}{2}}^{+K^+} \right) \right]$ $C_{k-\frac{1}{2}}^{+K_{k-1/2}^+} = \frac{\left w_{k-\frac{1}{2}}^{n+\alpha} \right \Delta t - \sum_{l=0}^{K_{k-1/2}^+ - 1} \Delta p_{k+l}}{\Delta p_{k+K_{k-1/2}^+}^n}$ <p>$\mathbf{w}_\eta > \mathbf{0}$ ($\mathbf{w} < \mathbf{0}$, physical downwelling)</p>	<p>$\mathbf{w} > \mathbf{0}$, physical upwelling</p> $F_{k-\frac{1}{2}}^n = \sum_{l=0}^{K_{k-1/2}^+ - 1} \left(\frac{\bar{q}_{k+l} \bar{\rho}_{k-1/2}^{n+1/2} \Delta z_{k+l}}{\Delta t} \right) + \frac{\bar{\rho}_{k-1/2}^{n+1/2} \Delta z_{k+K_{k-1/2}^+}}{\Delta t} C_{k-1/2}^{+K^+}$ $\left[\bar{q}_{k+K_{k-1/2}^+}^n + \frac{1}{2} \frac{\partial q}{\partial z} \Big _{k+K_{k-1/2}^+} \Delta z_{k+K_{k-1/2}^+} \left(1 - C_{k-\frac{1}{2}}^{+K^+} \right) \right]$ $C_{k-\frac{1}{2}}^{+K_{k-1/2}^+} = \frac{\left w_{k-\frac{1}{2}}^{n+1/2} \right \Delta t - \sum_{l=0}^{K_{k-1/2}^+ - 1} \Delta z_{k+l}}{\Delta z_{k+K_{k-1/2}^+}^n}$ <p>$\mathbf{w} < \mathbf{0}$, physical downwelling</p>

continued on the next page

Table 1.2: Courant number independent version of vertical MUSCL for ICOHAM and ICONAM

part	ICOHAM	ICONAM
	$F_{k-\frac{1}{2}}^n = \sum_{l=0}^{K_{k-1/2}^- - 1} \left(\bar{q}_{k-1-l} \frac{\Delta p_{k-1-l}}{\Delta t} \right) + \frac{\Delta p_{k-1-K_{k-1/2}^-}}{\Delta t} C_{k-1/2}^{-K_{k-1/2}^-}$ $\left[\bar{q}_{k-1-K_{k-1/2}^-}^n + \frac{1}{2} \frac{\partial q}{\partial p} \Big _{k-1-K_{k-1/2}^-} \right] \left[\bar{q}_{k-1-K_{k-1/2}^-}^n - \frac{1}{2} \frac{\partial q}{\partial z} \Big _{k-1-K_{k-1/2}^-} \right] \Delta z_{k-1-K_{k-1/2}^-}^n \left(1 - C_{k-\frac{1}{2}}^{-K_{k-\frac{1}{2}}^-} \right)$	$F_{k-\frac{1}{2}}^n = \sum_{l=0}^{K_{k-1/2}^- - 1} \left(- \frac{\bar{q}_{k-1-l} \Delta z_{k-1-l}^n}{\Delta t} \right) - \frac{\bar{\rho}_{k-1/2}^{-n+1/2} \Delta z_{k-1-K_{k-1/2}^-}^n}{\Delta t} C_{k-1/2}^{-K_{k-1/2}^-}$
vertical gradient	$C_{k-\frac{1}{2}}^{-K_{k-1/2}^-} = \frac{\left w_{k-\frac{1}{2}}^{n+\alpha} \right \Delta t - \sum_{l=0}^{K_{k-1/2}^- - 1} \Delta p_{k-1-l}}{\Delta p_{k-1-K_{k-1/2}^-}^n}$	$C_{k-\frac{1}{2}}^{-K_{k-1/2}^-} = \frac{\left w_{k-\frac{1}{2}}^{n+1/2} \right \Delta t - \sum_{l=0}^{K_{k-1/2}^- - 1} \Delta z_{k-1-l}}{\Delta z_{k-1-K_{k-1/2}^-}^n}$
linear interpolation from full level to half level	$q_{k-\frac{1}{2}}^n = \alpha_{k-\frac{1}{2}}^+ q_{k-\frac{1}{2}}^n + \alpha_{k-\frac{1}{2}}^- q_{k-1}^n$ $\alpha_{k-\frac{1}{2}}^+ = \frac{p_{k-\frac{1}{2}} - p_{k-1}}{p_{k-\frac{1}{2}} - p_{k-1}} \quad \alpha_{k-\frac{1}{2}}^- = \frac{p_{k-\frac{1}{2}} - p_{k-\frac{1}{2}}}{p_{k-\frac{1}{2}} - p_{k-1}}$ $\alpha_{k-\frac{1}{2}}^+ + \alpha_{k-\frac{1}{2}}^- = 1$	$q_{k-\frac{1}{2}}^n = \alpha_{k-\frac{1}{2}}^+ q_{k-\frac{1}{2}}^n + \alpha_{k-\frac{1}{2}}^- q_{k-1}^n$ $\alpha_{k-\frac{1}{2}}^+ = \frac{z_{k-1} - z_{k-\frac{1}{2}}}{z_{k-1} - z_k} \quad \alpha_{k-\frac{1}{2}}^- = \frac{z_{k-\frac{1}{2}} - z_k}{z_{k-1} - z_k}$ $\alpha_{k-\frac{1}{2}}^+ + \alpha_{k-\frac{1}{2}}^- = 1$

By introducing the coefficient \tilde{C} , with

$$\tilde{C} = \begin{cases} 1 & \text{if hydrostatic} \\ -1 & \text{if non-hydrostatic} \end{cases} \quad (1.72)$$

the two distinct formulations in table 1.1 can be condensed into one. Thus the same source code can be applied for both the height-based and pressure-based vertical coordinate system. The generalized transport scheme is given in table 1.3.. Serveral new variables have been introduced, i.e. $\Delta\xi_k^n$, $\tilde{F}_{\xi_{k-\frac{1}{2}}}^{n+\alpha}$, $w_{\xi_{k-\frac{1}{2}}}^{n+\alpha}$. Their meaning depends on the applied dyamical core. Table 1.4 provides a definition of those variables.

Table 1.3: Unified vertical MUSCL scheme for ICOHAM and ICONAM

part	ICOHAM and ICONAM
Time discretization	$\bar{q}_k^{n+1} = \bar{q}_k^n \frac{\bar{\rho}_k^n}{\bar{\rho}_k^{n+1}} - \tilde{C} \frac{\Delta t}{\bar{\rho}_k^{n+1}} \left[F_{k+\frac{1}{2}}^n - F_{k-\frac{1}{2}}^n \right]$
cell height	$\Delta\xi_k^n = \tilde{C} (\xi_{k+\frac{1}{2}}^n - \xi_{k-\frac{1}{2}}^n)$
Fluxes	<p>physical upwelling: $w_\eta < 0$, $w > 0$</p> $F_{k-\frac{1}{2}}^n = \tilde{F}_{\xi_{k-\frac{1}{2}}}^{n+\alpha} \left[\bar{q}_k^n - \tilde{C} \frac{1}{2} \frac{\partial q}{\partial \xi} \Big _k^n \Delta\xi_k^n \left(1 - C_{k-\frac{1}{2}}^+ \right) \right]$ $C_{k-\frac{1}{2}}^+ = \frac{ w_{\xi_{k-\frac{1}{2}}}^{n+\alpha} \Delta t}{\Delta\xi_k^n}$ <p>physical downwelling: $w_\eta > 0$, $w < 0$</p> $F_{k-\frac{1}{2}}^n = \tilde{F}_{\xi_{k-\frac{1}{2}}}^{n+\alpha} \left[\bar{q}_{k-1}^n + \tilde{C} \frac{1}{2} \frac{\partial q}{\partial \xi} \Big _{k-1}^n \Delta\xi_{k-1}^n \left(1 - C_{k-\frac{1}{2}}^- \right) \right]$ $C_{k-\frac{1}{2}}^- = \frac{ w_{\xi_{k-\frac{1}{2}}}^{n+\alpha} \Delta t}{\Delta\xi_{k-1}^n}$
vertical gradient	$\frac{\partial q}{\partial \xi} \Big _k^n = \tilde{C} \left(\frac{q_{k+\frac{1}{2}}^n - q_{k-\frac{1}{2}}^n}{\Delta\xi_k^n} \right)$
linear interpolation from fl to hl	$q_{k-\frac{1}{2}}^n = \alpha_{k-\frac{1}{2}}^+ q_k^n + \alpha_{k-\frac{1}{2}}^- q_{k-1}^n$ $\alpha_{k-\frac{1}{2}}^+ = \frac{\xi_{k-\frac{1}{2}} - \xi_{k-1}}{\xi_k - \xi_{k-1}} \quad \alpha_{k-\frac{1}{2}}^- = \frac{\xi_k - \xi_{k-\frac{1}{2}}}{\xi_k - \xi_{k-1}}$ $\alpha_{k-\frac{1}{2}}^+ + \alpha_{k-\frac{1}{2}}^- = 1$

Table 1.4: Definition of various variables which are introduced for the generalized vertical transport scheme

Variable	ICOHAM	units	ICONAM	units
ξ	p	Pa	z	m
mass flux \tilde{F}	$(\dot{\eta} \frac{\partial p}{\partial \eta})^{n+\alpha}$	$Pa s^{-1}$	$\rho^{n+1/2} w^{n+1/2}$	$kg m^{-2} s^{-1}$
vertical velocity w_ξ	$(\dot{\eta} \frac{\partial p}{\partial \eta})^{n+\alpha}$	$Pa s^{-1}$	$w^{n+1/2}$	$m s^{-1}$
density $\hat{\rho}$	Δp	$N m^{-2}$	$\rho \Delta z$	$kg m^{-2}$

1.4.2 Piecewise parabolic method (PPM)

The Piecewise parabolic method has been developed by Colella and Woodward (1984). It uses a piecewise parabolic function to approximate the unknown subgrid distribution of a 1D scalar field $q(z)$. The function is forced to be continuous between cells. Its construction is based on the known cell averages \bar{q}_k .

Mathematical formulation

Table 1.5 compares the third order vertical advection scheme for ICOHAM and ICONAM. The computation of the interface values $q_{k-1/2}^n$ is not presented. The computation follows the paper of Colella and Woodward (1984) and is done in the same way for both the height and pressure-based vertical coordinate system. An enhanced version, which is stable for $CFL > 1$ is presented in table 1.6. Unified versions that work for both the pressure-based and height-based vertical coordinate system are presented in 1.7 and 1.9. As for the vertical MUSCL scheme, the coefficient \tilde{C} equals 1 in the hydrostatic and -1 in the nonhydrostatic model.

Table 1.5: Comparison of PPM vertical advection for ICOHAM and ICONAM

part	ICOHAM	ICONAM
Time discretization	$\bar{q}_k^{n+1} = \bar{q}_k^n \frac{\Delta p_k^n}{\Delta p_k^{n+1}} - \frac{\Delta t}{\Delta p_k^{n+1}} \left[F_{k+\frac{1}{2}}^n - F_{k-\frac{1}{2}}^n \right]$	$\bar{q}_k^{n+1} = \bar{q}_k^n \frac{\bar{\rho}_k^n \Delta z_k}{\bar{\rho}_k^{n+1} \Delta z_k} - \frac{\Delta t}{\bar{\rho}_k^{n+1} \Delta z_k} \left[F_{k-\frac{1}{2}}^n - F_{k+\frac{1}{2}}^n \right]$
vertical velocity	$w_\eta = \dot{\eta} \frac{\partial p}{\partial \eta}$	$w = \dot{z}$
cell height	$\Delta p_k^n = p_{k+\frac{1}{2}}^n - p_{k-\frac{1}{2}}^n$	$\Delta z_k = z_{k-\frac{1}{2}} - z_{k+\frac{1}{2}}$
Fluxes	<p>$w_\eta < 0$ ($\mathbf{w} > 0$, physical upwelling)</p> $F_{k-\frac{1}{2}}^n = w_{\eta, k-\frac{1}{2}}^{n+\alpha} \left[\bar{q}_k^n - \frac{1}{2} \Delta q_k \left(1 - C_{k-1/2}^+ \right) \right] - \frac{1}{6} a_{6,k} \left(1 - 3C_{k-1/2}^+ + 2C_{k-1/2}^{+2} \right)$	<p>$\mathbf{w} > 0$ physical upwelling</p> $F_{k-\frac{1}{2}}^n = \bar{\rho}_{k-\frac{1}{2}}^{n+1/2} w_{k-\frac{1}{2}}^{n+1/2} \left[\bar{q}_k^n + \frac{1}{2} \Delta q_k \left(1 - C_{k-1/2}^+ \right) \right] - \frac{1}{6} a_{6,k} \left(1 - 3C_{k-1/2}^+ + 2C_{k-1/2}^{+2} \right)$

continued on the next page

Table 1.5: Comparison of PPM vertical advection for ICOHAM and ICONAM

part	ICOHAM	ICONAM
	$w_\eta > 0$ ($w < 0$, physical downwelling) $F_{k-\frac{1}{2}}^n = w_{\eta, k-\frac{1}{2}}^{n+\alpha} \left[\bar{q}_{k-1}^n + \frac{1}{2} \Delta q_{k-1} \left(1 - C_{k-1/2}^- \right) - \frac{1}{6} a_{6,k-1} \left(1 - 3C_{k-1/2}^- + 2C_{k-1/2}^{-2} \right) \right]$	$w < 0$ physical downwelling $F_{k-\frac{1}{2}}^n = \bar{p}_{k-\frac{1}{2}}^{n+1/2} w_{k-\frac{1}{2}}^{n+1/2} \left[\bar{q}_{k-1}^n - \frac{1}{2} \Delta q_{k-1} \left(1 - C_{k-1/2}^- \right) - \frac{1}{6} a_{6,k-1} \left(1 - 3C_{k-1/2}^- + 2C_{k-1/2}^{-2} \right) \right]$
Δq	$\Delta q_k^n = \bar{q}_{k+\frac{1}{2}}^n - \bar{q}_{k-\frac{1}{2}}^n$	$\Delta q_k^n = \bar{q}_{k-\frac{1}{2}}^n - \bar{q}_{k+\frac{1}{2}}^n$
a_6	$a_{6,k} = 6 \left[\bar{q}_k^n - \frac{1}{2} \left(\bar{q}_{k-\frac{1}{2}}^n + \bar{q}_{k+\frac{1}{2}}^n \right) \right]$	$a_{6,k} = 6 \left[\bar{q}_k^n - \frac{1}{2} \left(\bar{q}_{k-\frac{1}{2}}^n + \bar{q}_{k+\frac{1}{2}}^n \right) \right]$
Courant number	$C_{k-\frac{1}{2}}^+ = \frac{ w_\eta _{k-\frac{1}{2}}^{n+\frac{1}{2}} \Delta t}{\Delta p_k^n}$	$C_{k-\frac{1}{2}}^+ = \frac{ w _{k-\frac{1}{2}}^{n+\frac{1}{2}} \Delta t}{\Delta z_k}$
Courant number	$C_{k-\frac{1}{2}}^- = \frac{ w_\eta _{k-\frac{1}{2}}^{n+\frac{1}{2}} \Delta t}{\Delta p_{k-1}^n}$	$C_{k-\frac{1}{2}}^- = \frac{ w _{k-\frac{1}{2}}^{n+\frac{1}{2}} \Delta t}{\Delta z_{k-1}}$

Table 1.6: Comparison of Courant number independent PPM vertical advection for ICOHAM and ICONAM

part	ICOHAM	ICONAM
time discretization	$\bar{q}_k^{n+1} = \bar{q}_k^n \frac{\Delta p_k^n}{\Delta p_k^{n+1}} - \frac{\Delta t}{\Delta p_k^{n+1}} \left[F_{k+\frac{1}{2}}^n - F_{k-\frac{1}{2}}^n \right]$	$\bar{q}_k^{n+1} = \bar{q}_k^n \frac{\bar{p}_k^n \Delta z_k}{\bar{p}_k^{n+1} \Delta z_k} - \frac{\Delta t}{\bar{p}_k^{n+1} \Delta z_k} \left[F_{k-\frac{1}{2}}^n - F_{k+\frac{1}{2}}^n \right]$
vertical velocity	$w_\eta = \eta \frac{\partial p}{\partial \eta}$	$w = \dot{z}$
cell height	$\Delta p_k^n = p_{k+\frac{1}{2}}^n - p_{k-\frac{1}{2}}^n$	$\Delta z_k = z_{k-\frac{1}{2}} - z_{k+\frac{1}{2}}$
fluxes	<p>$w_\eta < 0$ ($w > 0$, physical upwelling)</p> $F_{k-\frac{1}{2}}^n = -\frac{1}{\Delta t} \left[\sum_{l=1}^{s(s>0)} (\Delta p^n \bar{q}^n)_{k+l-1} + F_{k-\frac{1}{2}+s}^{\text{frac}}(\bar{q}^n) \right]$ $F_{k-\frac{1}{2}+s}^{\text{frac}} = \Delta p_{k+s}^n \mu_{k-\frac{1}{2}}^{\text{frac}} \left[\bar{q}_{k+s}^n - \frac{1}{2} \Delta q_{k+s}^n \left(1 - \mu_{k-\frac{1}{2}}^{\text{frac}} \right) \right] - \frac{1}{6} a_{6,k+s} \left(1 - 3\mu_{k-\frac{1}{2}}^{\text{frac}} + 2\mu_{k-\frac{1}{2}}^{\text{frac} 2} \right)$	<p>$w > 0$ physical upwelling</p> $F_{k-\frac{1}{2}}^n = \frac{1}{\Delta t} \left[\sum_{l=1}^{s(s>0)} (\bar{p}^n \Delta z \bar{q}^n)_{k+l-1} + F_{k-\frac{1}{2}+s}^{\text{frac}}(\bar{q}^n) \right]$ $F_{k-\frac{1}{2}+s}^{\text{frac}} = \bar{p}_{k+s}^n \Delta z_{k+s} \mu_{k-\frac{1}{2}}^{\text{frac}} \left[\bar{q}_{k+s}^n + \frac{1}{2} \Delta q_{k+s}^n \left(1 - \mu_{k-\frac{1}{2}}^{\text{frac}} \right) \right] - \frac{1}{6} a_{6,k+s} \left(1 - 3\mu_{k-\frac{1}{2}}^{\text{frac}} + 2\mu_{k-\frac{1}{2}}^{\text{frac} 2} \right)$

continued on the next page

Table 1.6: Comparison of Courant number independent PPM vertical advection for ICOHAM and ICONAM

part	ICOHAM	ICONAM
	$w_\eta > 0$ ($w < 0$, physical downwelling) $F_{k-\frac{1}{2}}^n = \frac{1}{\Delta t} \left[\sum_{l=1}^{s(s>0)} (\Delta p^n \bar{q}^n)_{k-l} + F_{k-\frac{1}{2}-s}^{\text{frac}}(\bar{q}^n) \right]$ $F_{k-\frac{1}{2}+s}^n = \Delta p_{k-1-s}^n \mu_{k-\frac{1}{2}}^- \left[\bar{q}_{k-1-s}^n + \frac{1}{2} \Delta q_{k-1-s}^n \right] \left(1 - \mu_{k-\frac{1}{2}}^- \right)$ $- \frac{1}{6} a_{6,k-1-s} \left(1 - 3\mu_{k-\frac{1}{2}}^- \text{frac} + 2\mu_{k-\frac{1}{2}}^- \text{frac} 2 \right)$	$w < 0$ physical downwelling $F_{k-\frac{1}{2}}^n = -\frac{1}{\Delta t} \left[\sum_{l=1}^{s(s>0)} (\bar{p}^n \Delta z \bar{q}^n)_{k-l} + F_{k-\frac{1}{2}-s}^{\text{frac}}(\bar{q}^n) \right]$ $F_{k-\frac{1}{2}+s}^n = \bar{p}_{k-1-s}^n \Delta z_{k-1-s} \mu_{k-\frac{1}{2}}^- \left[\bar{q}_{k-1-s}^n + \frac{1}{2} \Delta q_{k-1-s}^n \right] \left(1 - \mu_{k-\frac{1}{2}}^- \text{frac} \right)$ $- \frac{1}{6} a_{6,k-1-s} \left(1 - 3\mu_{k-\frac{1}{2}}^- \text{frac} + 2\mu_{k-\frac{1}{2}}^- \text{frac} 2 \right)$
Δq	$\Delta q_k^n = \bar{q}_{k+\frac{1}{2}}^n - \bar{q}_{k-\frac{1}{2}}^n$	$\Delta q_k^n = \bar{q}_{k-\frac{1}{2}}^n - \bar{q}_{k+\frac{1}{2}}^n$
a_6	$a_{6,k} = 6 \left[\bar{q}_k^n - \frac{1}{2} \left(\bar{q}_{k-\frac{1}{2}}^n + \bar{q}_{k+\frac{1}{2}}^n \right) \right]$	$a_{6,k} = 6 \left[\bar{q}_k^n - \frac{1}{2} \left(\bar{q}_{k-\frac{1}{2}}^n + \bar{q}_{k+\frac{1}{2}}^n \right) \right]$
Courant number	$\mu_{k-\frac{1}{2}}^+ \text{frac} = \frac{ w_\eta _{k-\frac{1}{2}}^{n+\frac{1}{2}} \Delta t - \sum_{l=1}^{s(s>0)} \Delta p_{k+l-1}^n}{\Delta p_{k+s}^n}$	$\mu_{k-\frac{1}{2}}^+ \text{frac} = \frac{ \rho w _{k-\frac{1}{2}}^{n+\frac{1}{2}} \Delta t - \sum_{l=1}^{s(s>0)} (\bar{p}^n \Delta z)_{k+l-1}}{\bar{p}_{k+s}^n \Delta z_{k+s}}$
Courant number	$\mu_{k-\frac{1}{2}}^- \text{frac} = \frac{ w_\eta _{k-\frac{1}{2}}^{n+\frac{1}{2}} \Delta t - \sum_{l=1}^{s(s>0)} \Delta p_{k-l}^n}{\Delta p_{k-s-1}^n}$	$\mu_{k-\frac{1}{2}}^- \text{frac} = \frac{ \rho w _{k-\frac{1}{2}}^{n+\frac{1}{2}} \Delta t - \sum_{l=1}^{s(s>0)} (\bar{p}^n \Delta z)_{k-l}}{\bar{p}_{k-s-1}^n \Delta z_{k-s-1}}$

Table 1.7: Unified vertical PPM scheme for ICOHAM and ICONAM

part	ICOHAM and ICONAM
Time discretization	$\bar{q}_k^{n+1} = \bar{q}_k^n \frac{\hat{\rho}_k^n}{\hat{\rho}_k^{n+1}} - \tilde{C} \frac{\Delta t}{\hat{\rho}_k^{n+1}} \left[F_{k+\frac{1}{2}}^n - F_{k-\frac{1}{2}}^n \right]$
cell height	$\Delta \xi_k^n = \tilde{C} (\xi_{k+\frac{1}{2}}^n - \xi_{k-\frac{1}{2}}^n)$
Fluxes	<p>physical upwelling: $w_\eta < 0, \quad \mathbf{w} > \mathbf{0}$</p> $F_{k-\frac{1}{2}}^n = \tilde{F}_{\xi_{k-\frac{1}{2}}}^{n+\alpha} \left[\bar{q}_k^n - \tilde{C} \frac{1}{2} \Delta q_k \left(1 - C_{k-1/2}^+ \right) - \frac{1}{6} a_{6,k} \left(1 - 3C_{k-1/2}^+ + 2C_{k-1/2}^{+2} \right) \right]$ $C_{k-\frac{1}{2}}^+ = \frac{ w_{\xi_{k-\frac{1}{2}}}^{n+\alpha} \Delta t}{\Delta \xi_k^n}$ <p>physical downwelling: $w_\eta > 0, \quad \mathbf{w} < \mathbf{0}$</p> $F_{k-\frac{1}{2}}^n = \tilde{F}_{\xi_{k-\frac{1}{2}}}^{n+\alpha} \left[\bar{q}_{k-1}^n + \tilde{C} \frac{1}{2} \Delta q_{k-1} \left(1 - C_{k-1/2}^- \right) - \frac{1}{6} a_{6,k-1} \left(1 - 3C_{k-1/2}^- + 2C_{k-1/2}^{-2} \right) \right]$ $C_{k-\frac{1}{2}}^- = \frac{ w_{\xi_{k-\frac{1}{2}}}^{n+\alpha} \Delta t}{\Delta \xi_{k-1}^n}$
Δq	$\Delta q_k^n = \tilde{C} \left(q_{k+\frac{1}{2}}^n - q_{k-\frac{1}{2}}^n \right)$
$a_{6,k}$	$a_{6,k} = 6 \left(q_k^n - \frac{1}{2} (q_{k+1/2} + q_{k-1/2}) \right)$

Table 1.8: Definition of various variables which are introduced for the generalized vertical transport scheme

Variable	ICOHAM	units	ICONAM	units
ξ	p	Pa	z	m
mass flux \tilde{F}	$(\dot{\eta} \frac{\partial p}{\partial \eta})^{n+\alpha}$	$Pa s^{-1}$	$\rho^{n+1/2} w^{n+1/2}$	$kg m^{-2} s^{-1}$
vertical velocity w_ξ	$(\dot{\eta} \frac{\partial p}{\partial \eta})^{n+\alpha}$	$Pa s^{-1}$	$w^{n+1/2}$	$m s^{-1}$
density $\hat{\rho}$	Δp	$N m^{-2}$	$\rho \Delta z$	$kg m^{-2}$

Table 1.9: Unified Courant number independent vertical PPM scheme for ICOHAM and ICONAM

part	ICOHAM and ICONAM
Time discretization	$\bar{q}_k^{n+1} = \bar{q}_k^n \frac{\Delta m_k^n}{\Delta m_k^{n+1}} - \tilde{C} \frac{\Delta t}{\Delta m_k^{n+1}} \left[F_{k+\frac{1}{2}}^n - F_{k-\frac{1}{2}}^n \right]$
cell height	$\Delta \xi_k^n = \tilde{C} (\xi_{k+\frac{1}{2}}^n - \xi_{k-\frac{1}{2}}^n)$
Fluxes	<p style="text-align: center;">physical upwelling: $\tilde{F}_\eta < 0$, $\tilde{F}_z > 0$</p> $F_{k-\frac{1}{2}}^n = -\tilde{C} \frac{1}{\Delta t} \left[\sum_{l=1}^{s(s>0)} (\Delta m^n \bar{q}^n)_{k+l-1} + F_{k-\frac{1}{2}+s}^{\text{frac}}(\bar{q}^n) \right]$ $F_{k-\frac{1}{2}+s}^{\text{frac}} = \Delta m_{k+s}^n \mu_{k-\frac{1}{2}}^{+\text{frac}} \left[\bar{q}_{k+s}^n - \tilde{C} \frac{1}{2} \Delta q_{k+s}^n \left(1 - \mu_{k-\frac{1}{2}}^{+\text{frac}} \right) - \frac{1}{6} a_{6,k+s} \left(1 - 3\mu_{k-\frac{1}{2}}^{+\text{frac}} + 2\mu_{k-\frac{1}{2}}^{+\text{frac} 2} \right) \right]$

continued on the next page

Table 1.9: Unified Courant number independent vertical PPM scheme for ICOHAM and ICONAM

part	ICOHAM and ICONAM
	<p style="text-align: center;">physical downwelling: $\tilde{\mathbf{F}}_\eta > \mathbf{0}$, $\tilde{\mathbf{F}}_z < \mathbf{0}$</p> $F_{k-\frac{1}{2}}^n = \tilde{C} \frac{1}{\Delta t} \left[\sum_{l=1}^{s(s>0)} (\Delta m^n \bar{q}^n)_{k-l} + F_{k-\frac{1}{2}-s}^{\text{frac}}(\bar{q}^n) \right]$ $F_{k-\frac{1}{2}-s}^{\text{frac}} = \Delta m_{k-1-s}^n \mu_{k-\frac{1}{2}}^{-\text{frac}} \left[\bar{q}_{k-1-s}^n + \tilde{C} \frac{1}{2} \Delta q_{k-1-s}^n \left(1 - \mu_{k-\frac{1}{2}}^{-\text{frac}} \right) - \frac{1}{6} a_{6,k-1-s} \left(1 - 3\mu_{k-\frac{1}{2}}^{-\text{frac}} + 2\mu_{k-\frac{1}{2}}^{-\text{frac}2} \right) \right]$
Courant number	$\mu_{k-\frac{1}{2}}^{+\text{frac}} = \frac{ \tilde{F} _{k-\frac{1}{2}}^{n+\frac{1}{2}} \Delta t - \sum_{l=1}^{s(s>0)} \Delta m_{k+l-1}^n}{\Delta m_{k+s}^n}$
Courant number	$\mu_{k-\frac{1}{2}}^{-\text{frac}} = \frac{ \tilde{F} _{k-\frac{1}{2}}^{n+\frac{1}{2}} \Delta t - \sum_{l=1}^{s(s>0)} \Delta m_{k-l}^n}{\Delta m_{k-s-1}^n}$
Δq	$\Delta q_k^n = \tilde{C} \left(q_{k+\frac{1}{2}}^n - q_{k-\frac{1}{2}}^n \right)$
$a_{6,k}$	$a_{6,k} = 6 \left(q_k^n - \frac{1}{2} (q_{k+1/2} + q_{k-1/2}) \right)$

Table 1.10: Definition of various variables which are introduced for the generalized vertical transport scheme

Variable	ICOHAM	units	ICONAM	units
ξ	p	Pa	z	m
mass flux $\tilde{F}_{k-\frac{1}{2}}$	$(\dot{\eta} \frac{\partial p}{\partial \eta})_{k-\frac{1}{2}}^{n+\alpha}$	$Pa s^{-1}$	$\rho_{k-\frac{1}{2}}^{n+1/2} w_{k-\frac{1}{2}}^{n+1/2}$	$kg m^{-2} s^{-1}$
1D cell mass Δm_k	Δp_k	$N m^{-2}$	$\rho_k \Delta z_k$	$kg m^{-2}$

1.5 Reduced calling frequency

Assuming explicit time stepping (as it is the case in ICONAM), the continuity equation for air and the momentum equation must obey the maximum allowable time-step restrictions imposed by the fastest waves in the system (i.e. sound waves). While the continuity equation for air is inherently coupled to the momentum equations, passive tracer transport equations can be solved in isolation given prescribed winds and air densities. Continuity equations for passive tracers lack fast wave modes (sound and gravity waves) and, thus, have less restrictive time step limitations. Given the large number of passive tracers in state of the art climate and NWP models, significant computational cost savings can be obtained by sub-cycling the solution of the density and momentum equation with respect to the tracer equations. Stated in another way, the tracer equations can be integrated with a much larger time step compared to the density and momentum equation. In doing so, care has to be taken in order to maintain the desired tracer-mass consistency.

In the following we neglect the fact that, for stability reasons, divergence averaging is applied to the continuity equation of air mass. Let us start with the continuity equation for air mass in FFSL-form. The solution $\bar{\rho}_i^{n+1}$ (i.e. after 1 sub-timestep) is formally given by

$$\bar{\rho}_i^{n+1} = \bar{\rho}_i^n - \frac{1}{\Delta A_i} \sum_{e=1}^3 s_i^e \times \iint_{a_i^e} \rho^n(x, y) dA \quad (1.73)$$

with $s_i^e = \text{sgn}(\vec{v} \cdot \vec{n})$ indicating in- or outflow. Assuming m_{sub} sub-timesteps Δt for the dynamics, the solution at $n + m_{sub}$ can be written as follows

$$\bar{\rho}_i^{n+m_{sub}} = \bar{\rho}_i^n - \frac{1}{\Delta A_i} \sum_{e=1}^3 \sum_{m=0}^{m_{sub}} \delta \rho_i^{e, n+m}, \quad (1.74)$$

where $\delta \rho_i^{e, n+m}$ denotes the flux of air mass across edge e during one sub-timestep Δt . Accordingly

$$\sum_{m=0}^{m_{sub}} \delta \rho_i^{e, n+m} \quad (1.75)$$

denotes the total, accumulated flux of air mass across edge e during $m_{sub} \Delta t$. $\delta \rho_i^{e, n+m}$ is shorthand for

$$\delta \rho_i^{e, n+m} = s_i^{e, n+m} \times \iint_{a_i^{e, n+m}} \rho(x, y)^{n+m} dA \quad (1.76)$$

with $a_i^{e, n+m}$ denoting the departure region for timestep $n + m$. In ICONAM $\delta \rho_i^{e, n+m}$ is computed as

$$\delta \rho_i^{e, n+m} = s_i^{e, n+m} \times \left(\Delta t l_i^e v_{n,i}^{e,x} \rho_i^{e,y} \right) \quad (1.77)$$

where Δt is the sub-timestep, l_i^e denotes the length of edge e for cell i , $v_{n,i}^{e,x}$ denotes the normal velocity component at edge e and ρ_i^e denotes the density interpolated to edge e . x and y are placeholder for not yet specified points in time, which depend on the time-integration scheme chosen for dynamics.

Now let's have a closer look at the continuity equation for a passive tracer. Assuming the same sub-timestep as for the air mass, the solution $\overline{\rho q_i^{n+1}}$ is formally given by

$$\overline{\rho q_i^{n+1}} = \overline{\rho q_i^n} + \frac{1}{\Delta A_i} \sum_{e=1}^3 \frac{1}{\Delta a_i^e} \iint_{a_i^e} q^n(x, y) \, dA \, \delta \rho_i^{e,n} \quad (1.78)$$

Here we assume that the mass flux is provided by the dynamical core. When updating tracers on the long time step $m_{sub}\Delta t$, tracer-mass consistency can be ensured when using time accumulated mass fluxes and time averaged wind fields. Thus, the solution of the transport equation over the long time step $m_{sub}\Delta t$ is given by

$$\overline{\rho q_i^{n+m_{sub}}} = \overline{\rho q_i^n} + \frac{1}{\Delta A_i} \sum_{e=1}^3 \langle q^n \rangle^e \sum_{m=1}^{m_{sub}} \delta \rho_i^{e,n+m} \quad (1.79)$$

The average $\langle q^n \rangle^e$ of the mixing ratio q^n is estimated over the long time-step $m_{sub}\Delta$ for each edge e .

$$\langle q^n \rangle^e = \frac{1}{\Delta \langle a_i^e \rangle} \iint_{\langle a_i^e \rangle} q^n(x, y) \, dA. \quad (1.80)$$

Note that $\langle a_i^e \rangle$ differs from a_i^e . The latter denotes the departure region corresponding to the sub-timestep Δt , while the former is the departure region corresponding to the full timestep $m_{sub}\Delta t$. For the computation of $\langle a_i^e \rangle$ the time-averaged wind field

$$\overline{v_n} = \frac{1}{mstep} \sum_{m=0}^{msteps-1} v_n^{n\pm x+m} \quad (1.81)$$

is used.

If $q = 1$, then (1.79) reduces to the equation for air mass (1.74) and, thus, tracer-mass consistency will be maintained.

For ICON it is planned to use $mstep = 4$. For the time being it is only implemented for the triangular version of ICONAM.

Chapter 2

Tracer transport in ICOHAM

Chapter 3

Transport

3.1 Argument lists

Argument lists of the following subroutines are documented below:

- `step_advection` (table 3.1)
- `vert_upwind_flux` (table 3.2)
- `hor_upwind_flux` (table 3.3)

Table 3.1: Argument list of driver subroutine `step_advection`

Name	physical variable		units		INTENT	description
	ICOHAM	ICONAM	ICOHAM	ICONAM		
<code>p_patch</code>	–	–	–	–	IN	patch on which computation is performed
<code>p_int_state</code>	–	–	–	–	IN	interpolation state
<code>p_dtime</code>	Δt	Δt	s	s	IN	time step
<code>k_step</code>	–	–	1	1	IN	time step counter
<code>p_tracer_now</code>	\bar{q}_k^n	\bar{q}_k^n	$kg\ kg^{-1}$	$kg\ kg^{-1}$	IN	4D tracer array
<code>p_mflx_contra_h</code>	$\Delta p^{n+\alpha} v_n^{n+\alpha}$	$\rho^{n+1/2} \Delta z v_n^{n+1/2}$	$kg\ s^{-3}$	$kg\ m^{-1}\ s^{-1}$	IN	horizontal mass flux at edge midpoints
<code>p_vn_contra_traj</code>	$v_n^{n+\alpha}$	$v_n^{n+1/2}$	$m\ s^{-1}$	$m\ s^{-1}$	IN	normal velocity component at edge midpoints
<code>p_mflx_contra_v</code>	$(\eta \frac{\partial v}{\partial \eta})_{k-1/2}^{n+\alpha}$	$\rho_{k-1/2}^{n+1/2} w_{k-1/2}^{n+1/2}$	$Pa\ s^{-1}$	$kg\ m^{-2}\ s^{-1}$	INOUT	contravariant vertical mass flux at half level centers
<code>p_w_contra_traj</code>	$(\eta \frac{\partial w}{\partial \eta})_{k-1/2}^{n+\alpha}$	$w_{k-1/2}^{n+1/2}$	$Pa\ s^{-1}$	$m\ s^{-1}$	IN	contravariant vertical velocity at half level centers
<code>p_cellhgt_mc_now</code>	Δp_k^n	Δz_k	Pa	m	IN	cell height at cell circumcenter
<code>p_delp_mc_new</code>	Δp_k^{n+1}	$\rho_k^{n+1} \Delta z_k$	Pa	$kg\ m^{-2}$	IN	new weighted density
<code>p_delp_mc_now</code>	Δp_k^n	$\rho_k^n \Delta z_k$	Pa	$kg\ m^{-2}$	IN	old weighted density
<code>p_pres_mc_now</code>	p_k^n	z_k	Pa	m	IN	full level height
<code>p_pres_ic_now</code>	$p_{k-1/2}^n$	$z_{k-1/2}$	Pa	m	IN	half level height
<code>p_grf_tend_tracer</code>	$\Delta t \frac{\partial q}{\partial t}$	$\Delta t \frac{\partial q}{\partial t}$	$kg\ kg^{-1}$	$kg\ kg^{-1}$	INOUT	interpolated tracer time tendencies

continued on the next page

Table 3.1: Argument list of driver subroutine `step_advecton`

Name	physical variable		units		INTENT	description
	ICOHAM	ICONAM	ICOHAM	ICONAM		
<code>p_tracer_new</code>	\bar{q}_k^{n+1}	\bar{q}_k^{n+1}	$kg\ kg^{-1}$	$kg\ kg^{-1}$	INOUT	updated 4D tracer array
<code>p_m_flux_tracer_h</code>	F_i^n	F_i^n	$kg\ s^{-3}$	$kg\ m^{-1}\ s^{-1}$	INOUT	horizontal tracer mass flux at edge midpoints
<code>p_m_flux_tracer_v</code>	$F_{k-1/2}^n$	$F_{k-1/2}^n$	$Pa\ s^{-1}$	$kg\ m^{-2}\ s^{-1}$	INOUT	vertical tracer mass flux at half level centers
<code>opt_rho_ic</code>	–	$\rho_{k-1/2}^{n+1/2}$	–	$kg\ m^{-3}$	OPT IN	half level density (NH-core only)
<code>opt_top_flux_tra</code>	–	$F_{1/2}^n$	$Pa\ s^{-1}$	$kg\ m^{-2}\ s^{-1}$	OPT IN	vertical tracer flux at upper boundary (NH-core only)
<code>opt_q_int</code>	–	$\bar{q}_{1/2}^n$	–	$kg\ kg^{-1}$	OPT OUT	tracer value at upper boundary of child nest (NH-core only)
<code>opt_ddt_tracer_adv</code>	$\frac{\partial q}{\partial t}$	$\frac{\partial q}{\partial t}$	$kg\ kg^{-1}\ s^{-1}$	$kg\ kg^{-1}\ s^{-1}$	OPT INOUT	advective tendency (NH-core only)

Table 3.2: Argument list of subroutine `vert_upwind_flux`

Name	physical variable		units		INTENT	description
	ICOHAM	ICONAM	ICOHAM	ICONAM		
<code>p_patch</code>	-	-	-	-	IN	patch on which computation is performed
<code>p_cc</code>	\bar{q}^n	\bar{q}^n	$kg\ kg^{-1}$	$kg\ kg^{-1}$	IN	advected cell centered variable (3D field)
<code>p_mflx_contra_v</code>	$(\frac{\partial p}{\partial \eta})^{n+\alpha}$	$\rho^{n+1/2} w^{n+1/2}$	$Pa\ s^{-1}$	$kg\ m^{-2}\ s^{-1}$	INOUT	contravariant vertical mass flux at half level centers
<code>p_w_contra</code>	$(\frac{\partial p}{\partial \eta})^{n+\alpha}$	$w^{n+1/2}$	$Pa\ s^{-1}$	$m\ s^{-1}$	IN	contravariant vertical velocity at half level centers
<code>p_dtime</code>	Δt	Δt	s	s	IN	time step
<code>p_pres_ic</code>	$p_{k-1/2}^n$	$z_{k-1/2}$	Pa	m	IN	half level height
<code>p_pres_mc</code>	p_k^n	z_k	Pa	m	IN	full level height
<code>p_cellhgt_mc_now</code>	Δp^n	Δz	Pa	m	IN	cell height at cell circumcenter
<code>p_rcellhgt_mc_now</code>	$1/\Delta p^n$	$1/\Delta z$	Pa^{-1}	m^{-1}	IN	reciprocal cell height at cell circumcenter
<code>p_cellmass_now</code>	Δp^n	$\rho^n \Delta z$	Pa	$kg\ m^{-2}$	IN	1D cell mass
<code>p_ivadv_tracer</code>	-	-	1	1	IN	selects numerical scheme for vertical transport
<code>p_itype_vlimit</code>	-	-	1	1	IN	selects limiter for vertical transport
<code>p_ivbc_adv</code>	-	-	1	1	IN	selects upper boundary condition
<code>p_iadv_slev</code>	-	-	1	1	IN	vertical start level
<code>p_upflux</code>	$F_{k-1/2}^n$	$F_{k-1/2}^n$	$Pa\ s^{-1}$	$kg\ m^{-2}\ s^{-1}$	OUT	vertical tracer mass flux at half level centers

continued on the next page

Table 3.2: Argument list of subroutine `vert_upwind_flux`

Name	physical variable		units		INTENT	description
	ICOHAM	ICONAM	ICOHAM	ICONAM		
<i>opt_topflux_tra</i>	–	$F_{1/2}^n$	–	$kg\ m^{-2}\ s^{-1}$	IN	vertical tracer flux at upper boundary (NH core only)
<i>opt_q_int</i>	–	$\bar{q}_{1/2}^n$	–	$kg\ kg^{-1}$	OUT	tracer value at upper boundary of child nest (NH core only)
<i>opt_rho_ic</i>	–	$\rho_{k-1/2}^{n+1/2}$	–	$kg\ m^{-3}$	OPT IN	half level density (NH-core only)
<i>opt_rstart</i>	–	–	1	1	OPT IN	refinement control start level
<i>opt_rlend</i>	–	–	1	1	OPT IN	refinement control end level

Table 3.3: Argument list of subroutine `hor_upwind_flux`

Name	physical variable		units		INTENT	description
	ICOHAM	ICONAM	ICOHAM	ICONAM		
<code>p_cc</code>	\bar{q}^n	\bar{q}^n	$kg\ kg^{-1}$	$kg\ kg^{-1}$	IN	advected cell centered variable (3D field)
<code>p_c0</code>	\bar{q}^n	\bar{q}^n	$kg\ kg^{-1}$	$kg\ kg^{-1}$	IN	advected cell centered variable (3D field) step (n)
<code>p_mass_flux_e</code>	$\Delta p^{n+\alpha} v_n^{n+\alpha}$	$\rho^{n+1/2} \Delta z v_n^{n+1/2}$	$kg\ s^{-3}$	$kg\ m^{-1}\ s^{-1}$	IN	horizontal mass flux at edge midpoints
<code>p_vn</code>	$v_n^{n+\alpha}$	$v_n^{n+1/2}$	$m\ s^{-1}$	$m\ s^{-1}$	IN	normal velocity component at edge midpoints
<code>p_dtime</code>	Δt	Δt	s	s	IN	time step
<code>p_patch</code>	—	—	—	—	IN	patch on which computation is performed
<code>p_int</code>	—	—	—	—	IN	interpolation state
<code>p_ihadv_tracer</code>	—	—	1	1	IN	selects numerical scheme for horizontal transport
<code>p_igrad_c_miura</code>	—	—	1	1	IN	selects gradient reconstruction method at cell centers
<code>p_itype_hlimit</code>	—	—	1	1	IN	selects limiter for horizontal transport
<code>p_iadv_slev</code>	—	—	1	1	IN	vertical start level
<code>p_iord_backtraj</code>	—	—	1	1	IN	selects method for backward trajectory computation
<code>p_upflux</code>	F_i^n	F_i^n	$kg\ s^{-3}$	$kg\ m^{-1}\ s^{-1}$	INOUT	horizontal tracer mass flux at edge
<code>opt_rlend</code>	—	—	1	1	OPT IN	refinement control end level

Bibliography

- Boris, J. P. and D. L. Book, 1973: Flux-corrected transport I: SHASTA, a fluid transport algorithm that works. *Journal of Computational Physics*, **11**, 38–69.
- Colella, P. and P. R. Woodward, 1984: The piecewise parabolic method (ppm) for gas-dynamical simulations. *Journal of Computational Physics*, **54**, 174–201.
- Easter, R. C., 1993: Two modified versions of Bott’s positive-definite numerical advection scheme. *Monthly Weather Review*, **121**, 297–304.
- Golub, G. H. and C. F. V. Loan, 1996: *Matrix Computations*. TeubnerJohns Hopkins University Press, 687, third edition.
- Harris, L. M. and P. H. Lauritzen, 2010: A flux-form version of the conservative semi-lagrangian multi-tracer transport scheme (cslam) on the cubed sphere grid. *Journal of Computational Physics*, **230**, 1215–1237.
- Lauritzen, P. H., C. Jablonowski, M. A. Taylor, and R. D. Nair, 2011: *Numerical Techniques for Global Atmospheric Models*. Springer, 556, first edition.
- Lauritzen, P. H., R. D. Nair, and P. A. Ullrich, 2010: A conservative semi-lagrangian multi-tracer transport scheme (cslam) on the cubed-sphere grid. *Journal of Computational Physics*, **229**, 1401–1424.
- Levy, M. N., R. D. Nair, and H. M. Tufo, 2007: High-order galerkin method for scalable global atmospheric models. *Computers and Geoscience*, **33**, 1022–1035.
- Lipscomb, W. H. and T. D. Ringler, 2005: An incremental remapping transport scheme on a spherical geodesic grid. *Monthly Weather Review*, **133**, 2335–2350.
- Miura, H., 2007: An upwind-biased conservative advection scheme for spherical hexagonal-pentagonal grids. *Monthly Weather Review*, **135**, 4038–4044.
- Nair, R. D. and P. H. Lauritzen, 2010: A class of deformational flow test cases for linear transport problems on the sphere. *Journal of Computational Physics*, **229**, 8868–8887.
- Skamarock, W. C. and M. Menchaca, 2010: Conservative transport schemes for spherical geodesic grids: High-order reconstructions for forward-in-time schemes. *Monthly Weather Review*, **138**, 4497–4508.
- Thuburn, J. and M. E. McIntyre, 1997: Numerical advection schemes, cross-isentropic random walks, and correlations between chemical species. *Journal of Geophysical Research*, **102**(D6), 6775–6797.

Yeh, K.-S., 2007: The streamline subgrid integration method: I. quasi-monotonic second order transport schemes. *Journal of Computational Physics*, **225**, 1632–1652.

Zalesak, S. T., 1979: Fully multidimensional flux-corrected transport algorithms for fluid. *Journal of Computational Physics*, **31**, 335–362.